ECHELLE SPECTROSCOPY OF THE NUCLEI OF THE HIGHLY COLLIMATED BIPOLAR PLANETARY NEBULAE M 2-9 AND M 1-91[1]

S. Torres-Peimbert,[2] A. Arrieta,[3] and M. Bautista[4]

RESUMEN

Presentamos espectroscopía echelle del núcleo sin resolver de las nebulosas bipolares M 2-9 and M 1-91. Los espectros están dominados por líneas de emisión emitidas en un amplio intervalo de condiciones físicas. De las observaciones identificamos las líneas de emisión, las condiciones físicas y los movimientos relativos de las diferentes especies ionizadas en la región circunestelar de ambos objetos. Proponemos que las líneas prohibidas observadas se originan en la parte interior del toro extendido que rodea a cada objeto.

ABSTRACT

We present echelle spectroscopy of the unresolved nuclei of the bipolar planetary nebulae M 2-9 and M 1-91. The spectrum is dominated by emission lines emitted under a wide range of physical conditions. From the observations we identify the emission lines, derive physical conditions and relative motions of the different ionized species in the circumstellar region of both objects. We propose that the observed forbidden lines arise in the inner part of the extended torus that surrounds each object.

Key Words: planetary nebulae: individual (M 2-9, M 1-91)

1. INTRODUCTION

Among the many interesting proto-planetary nebulae and young planetary nebulae there are those with extreme bipolar shape, or "butterfly" type. M 2-9 and M 1-91 are analogous not only in morphology, but also in dusty lobes and spectral characteristics of their nuclear regions. M 2-9 has been widely studied in many of its characteristics, and yet is not fully understood; the studies on M 1-91, have been more limited because it is considerably fainter, and thus it is less well understood. We present here the result of our spectroscopic observations of their central objects in an attempt to further understand the physical conditions of the circumstellar gas. In what follows we will present each of the objects, describe the observations and their characteristics. For M 2-9 we discuss the profiles of the Balmer lines, of

[O III] lines, and the intensities of the Fe lines. We also derive the reddening law and the behavior of its physical conditions as a function of velocity relative to the central star. For M 1-91 we carry out a similar study; however, as expected, the information derived for this object is more limited.

2. OBSERVATIONS

The observations were carried out at the Observatorio Astrónomico Nacional in San Pedro Mártir, Baja California with the 2.1 m telescope and the REOSC echelle spectrograph (R $\sim$ 18,000 at 5,000 Å) and a 1024 $\times$ 1024 Tektronix detector that yields a spectral resolution of 10.6 km s^{-1} and a spatial resolution of 0.99″ per pixel. The 3600 to 6850 Å range was covered in 29 orders (blue spectrum) for both objects, and the 6500 to 9500 Å range in 11 orders (red spectrum) for M 2-9.

Long slit observations, 79.8″ $\times$ 2″, oriented along the major axis were obtained for both objects. The exposure time for the blue spectrum of M 2-9 was 600 sec and the other spectra required 900 sec.

Short window extractions (10 pixels) were performed to obtain the nuclear spectra, which will be reported here. For M 2-9 the blue spectrum was

[2]Instituto de Astronomía, Universidad Nacional Autónoma de México, Mexico.

[3]Depto. de Física y Matemáticas, Universidad Iberoamericana, Mexico.

[4]Department of Physics, Western Michigan University, USA.

observed on 23 April 1995 and the red on 25 April 1995; while for M 1-91 the observations were carried out on 27 May 1998. The data reduction was carried out with IRAF routines. The spectra were normalized to the continuum for each spectral order with a Chebyshev polynomial.

3. M 2-9

One of the most interesting objects is M 2-9 (PN G10.8+18), a bright nebula of extreme bipolar morphology. It is seen almost face-on, with a size of approximately $12'' \times 48''$ and extensions that reach up to $60''$ from the nucleus (Schwarz et al. 1997). It has been extensively studied (cf. Allen & Swings 1972; Balick 1989; Hora & Latter 1994; Schwarz et al. 1997; Solf 2000; Doyle et al. 2000).

The evolutionary status of M 2-9 is still controversial. M 2-9 has been identified with objects which "bear the characteristics indicative for very young planetary nebulae", such as M 1-91, M 1-92 (Solf 1984), CRL 618 (Schmidt & Cohen 1981) or "proto-planetary nebulae" (Walsh 1981). Schwarz et al. (1997) derive a distance to M 2-9 of 650 pc. At this distance the bolometric luminosity is 550 $L_\odot$ and its dynamic age is 1200 years. So at least one Mira-containing symbiotic system is reminiscent of the odd behavior pattern of M 2-9 (Doyle et al. 2000).

The lobes are found to have a double shell structure; the outer shell is dominated by H_2 line emission (Hora & Latter 1994) The lobes have condensations symmetrically located relative to the equatorial plane. The weak emissions observed at $60''$ S and N of the nucleus are also located in a point-symmetric distribution. One of the more significant characteristics of this object is that the knots brighter and closer to the nucleus show motions parallel to the equatorial plane (Allen & Swings 1972; Kohoutek & Surdej 1980; Balick 1989; Doyle et al. 2000).

Polarimetric studies show that the radiation from the lobes is polarized, suggesting that the nebular emission has two components: one produced locally in the lobes and another one probably being light scattered from the bright central region (Trammell, Goodrich, & Dinerstein 1995).

Upon examination of direct HST images Balick (1999) found that the [O III] image shows a series of knots lying along the nebula's symmetry axis. Unlike other knots in the lobes, the near-nuclear [O III] knots have no counterparts in other emission lines. The enlarged [S II] image shows a network of nearly radial filaments that are not artifacts of the telescope optics. These are associated with the base of the lobes. Figure 1 shows an image of the bipolar
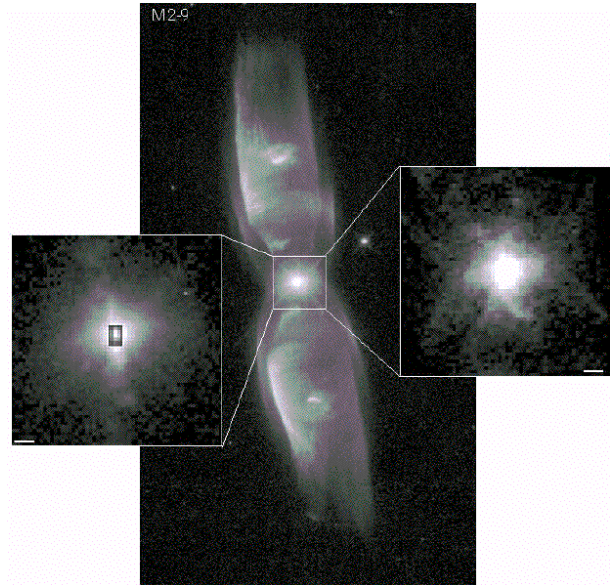

Fig. 1. HST image of the bipolar planetary nebula M 2-9 from Balick et al. (1997). Also shown are details of the internal region taken with two different filters: [OIII] on the left, and [S II] on the right.

nebula in the light of [O III] and [S II]. An enlargement of the central regions is presented (from Balick, Icke, & Mellema 1997).

3.1. *Nucleus of M 2-9*

M 2-9 is a very dust rich nebula. It has been found that the reddening of the nucleus is significantly different from that shown in the lobes. In the nucleus, different authors have found different reddening values; Swings & Andrillat (1979) and Calvet & Cohen (1978) determined an $A_v \geq 5$ mag, while Hora & Latter (1994) from the hydrogen Brackett series determined an $A_v = 2.3$ mag.

The nuclear spectrum shows nebular lines in emission over a weak continuum. No absorption lines have been observed, therefore the determination of its spectral type is very uncertain. It has been proposed that the nucleus is composed of a binary system: a hot component that ionizes the O^{++} gas and a B5 star that contributes to its visible luminosity (Calvet & Cohen 1978). Also Schwarz et al. (1997) suggest that a compact but hot component must be present; the hot component ionizes the high excitation emission lines while the B5 (or cooler) star provides part of the luminosity and the binary interaction of the pair produces the high collimation of the nebula. An accretion disk around the compact star would provide the fast disk wind.

Among other possible explanations, Livio & Soker (2001) have proposed a model to explain the apparent motion of the knots and the evolutionary stage of the exciting star. They propose that the nucleus is constituted by a binary system composed by an AGB or post-AGB star and a white dwarf.

Kwok et al. (1985) observed at five different radio continuum frequencies angular radii of the optically thick surface from 0.033″ to 22″, depending on the frequency. Adopting a value of the wind velocity of 1600 km s^{-1} they derive a mass loss rate of $3.3 \times 10^{-5}\,M_\odot$ yr^{-1} for a distance of 1 kpc. If the distance is 650 pc, then the mass loss rate is $1.1 \times 10^{-5}\,M_\odot$ yr^{-1}. This mass loss rate is much higher than the rates ($< 10^{-7}\,M_\odot$ yr^{-1}) estimated for other planetary nebulae. They propose that M 2-9 has descended from a rotating red-giant progenitor and that the bipolar morphology is the result of rapid expansion of the ionization front in the N-S directions.

Interferometric mapping of the ^{12}CO J = 1 - 0 emission from M 2-9 by Zweigle et al. (1997) indicates the existence of an expanding equatorial torus of molecular gas of about 6″ diameter around the center of M 2-9. The symmetry axis of the torus is tilted with respect to the plane of the sky by $\sim 17°$. The deprojected expansion velocity is 7 km s^{-1}, and for a distance of 650 pc, it corresponds to a kinematical age of about 1365 years.

Smith, Balick, & Gehrz (2005) using high dispersion near infrared spectra observe the 2.12 μm H$_2$ line and determine that the nuclear emission arises in an equatorial molecular disk or torus, consistent with the detection of a CO torus by Zweigle et al. (1997), where the H$_2$ emission arises closer to the central star, perhaps marking the irradiated inner edge of this larger torus.

Near-infrared color images of M 2-9 by Aspin, McLean, & Smith (1988) suggest that the central core of M 2-9 is surrounded by a dense extended equatorial disk of luminous dust. From the spectral energy distribution of the bright central core, using a 4″ diameter aperture, Smith & Gehrz (2005) fit a 260 K gray body to the unresolved central engine, although they suggest that the observed SED is actually flatter than any single temperature, perhaps indicating dust at various radii in a circumstellar disk.

3.2. *Systemic velocity*

The determination of the systemic velocity is not straightforward, since no photospheric lines are detected in the spectra of the nucleus of M 2-9. The emission lines show composite profiles or have different velocities depending on the degree of ionization,
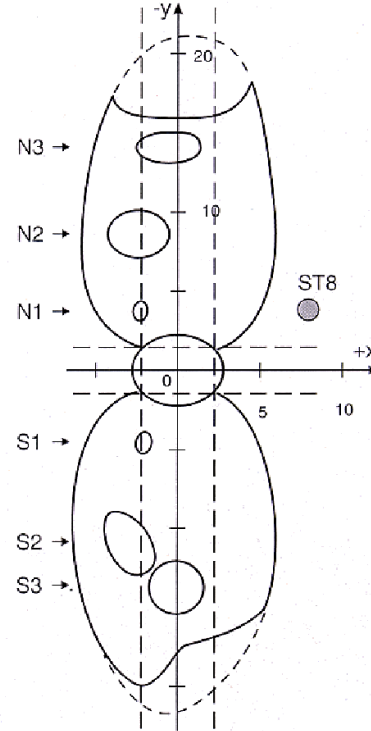
Fig. 2. Diagram of the structure of M 2-9 where the knots and nomenclature by Kohoutek & Surdej (1980) are shown. Also indicated is the position of the spectrograph slit used.

which allows us to assume that they are produced in circumstellar regions. Therefore, we determined the nuclear velocity from the kinematics of the lobes.

We show in Figure 2 the positions of the slit in the case of M 2-9, where we use the nomenclature by Kohoutek & Surdej (1980) to refer to the condensations. The detailed Hα profile was used to determine the systemic velocity.

On the long slit Hα spectral isocontours shown in Figure 3, a very bright central region with a double peak profile and two regions can be seen that correspond to the northern and southern lobes. Superimposed on the lobe emission, there are strong emissions at +15″ and –15″ relative to the nucleus, which correspond to the N3 and S3 knots, respectively. The nuclear velocity was estimated under the assumption that both knots were ejected symmetrically from the central region at the same speed.

In this figure the dashed line joins the intensity maxima of the N3 and S3 knots through the central region. The arrows indicate λ_0, the laboratory wavelength for Hα and the central part of the nebula. The velocity difference is $+40 \pm 5$ km s^{-1}, which yields a systemic heliocentric velocity of $+60\pm5$ km s^{-1} (cor-
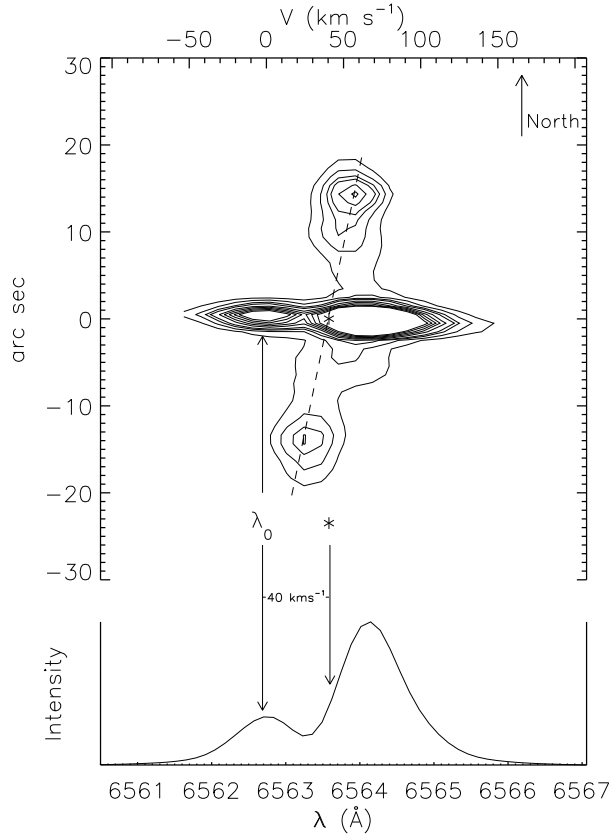
Fig. 3. Position-velocity diagram of the central part of M 2-9 from the long slit spectrum of the Hα profile. To determine the systemic velocity it has been assumed that the N3 and S3 knots were ejected symmetrically and are moving at the same speed relative to the nucleus. The dashed line joins both knots and yields the velocity of the nucleus. The laboratory wavelength of the derived velocity of the nucleus is indicated, which corresponds to a heliocentric velocity of $+60 \pm 5$ km s^{-1}.

responding to $V_{\mathrm{LSR}} = +75$ km s^{-1}). In the following sections all velocities will be referred to the systemic velocity. This value is comparable to those obtained by other authors; namely, $V_{\mathrm{hel}} = +69.2$ km s^{-1} from [Fe II] (Smith et al. 2005); and $V_{\mathrm{LSR}} = +80$ km s^{-1} from CO, (Bachiller, Martín-Pintado, & Bujarrabal 1990; Zweigle et al. 1997).

3.3. Spectrum Description

The nuclear spectrum is dominated by emission lines over a weak continuum, where no absorption lines can be detected; therefore it is not possible to determine directly the central star spectral type. In our data, emission lines from the following ions were identified and measured: H I, He I, C I, C II, C III, N I, N II, O I, O II, O III, Ne I, Ne II, Mg I, Mg II, Si I, Si II, Cl III, Ca I, Fe I, Fe II, Fe III, Ni II,

Ni III, [N I], [N II], [N IV], [O I], [O II], [O III], [Ne III], [S II], [S III], [Cl II], [Cl III], [Ar III], [Cr II], [Cr III], [Mn II], [Fe I], [Fe II], [Fe III], [Fe IV], [Ni II], [Ni III], and [Ni IV]. To identify the lines in this very rich spectrum we used the code EMILI (Sharpee et al. 2003) under a set of different temperatures (9,000 to 11,500 K) and densities (10^4 to 10^7 cm^{-3}) to account for the different conditions that prevail in the source. The blue spectrum from 4150 to 6850 Å is presented in Figure 4, and the red spectrum from 6500 to 9400 Å in Figure 5. In both figures the most intense features have been marked.

Some of these lines are emitted in different unresolved regions of different velocities. For example, the Balmer lines have two maxima with a stronger red component. Also the profiles of the [OIII] 4959,5007 Å lines show two maxima, but in this case the blue component is brighter. The rest of the lines are approximately symmetric about a single peak; at the spectral resolution available, they are adjusted satisfactorily with Gaussian profiles. Tables 1 and 2 list the identifications of the observed lines for the 3700 to 6800 Å range and for the 6450 to 9460 Å range, respectively. They contain in Columns (1) and (2) the laboratory and observed wavelengths of the identified lines; in Columns (3) and (4) the measured intensities relative to Hβ and the extinction corrected intensity (see details of the extinction law in § 3.4); in Column (5) the measured FWHM (uncorrected for instrumental width); and in Column (6) the line identification. The blue section is normalized to Hβ, while the red section has been normalized to Hα. It was not possible to normalize the red spectrum to Hβ because the observations were carried out on different nights under different atmospheric conditions.

3.4. Interstellar extinction

Usually the Balmer and Paschen line ratios are used to derive interstellar extinction to any object. M 2-9 poses a difficult case, since its hydrogen lines show very complex profiles. While the Balmer lines show double peaked profiles, the Paschen lines show single component lines. Figure 6 shows these profiles normalized to maximum intensity. In this figure, lines are shown in increasing order of the upper level of the transition for each series. In the Balmer series, the Hα line shows two well separated components and the separation becomes less well defined as the energy of the upper level increases.

On the other hand, the Paschen series shows essentially a single component. A possible explanation for the single components could be that at these
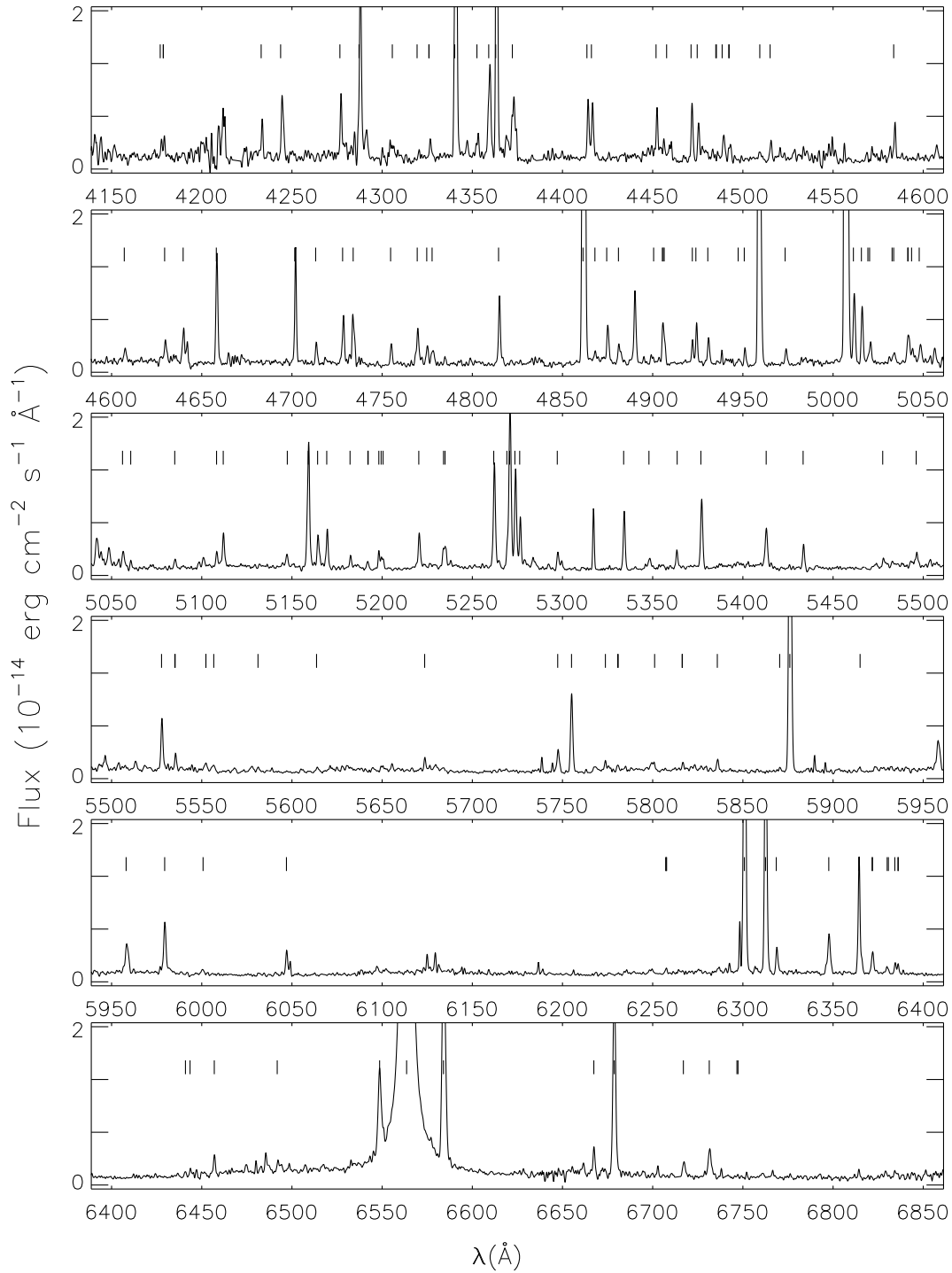
Fig. 4. Blue spectrum of the nucleus of M 2-9; it has been expanded to show the faint lines. The identified lines are indicated.

wavelengths the spectral resolution is lower than in the case of Hα. To rule out this possibility we degraded the resolution of the Balmer series to the same resolution as the Paschen series and found that the difference between the two peaks continues to be appreciable. Alternatively, if extinction were respon-
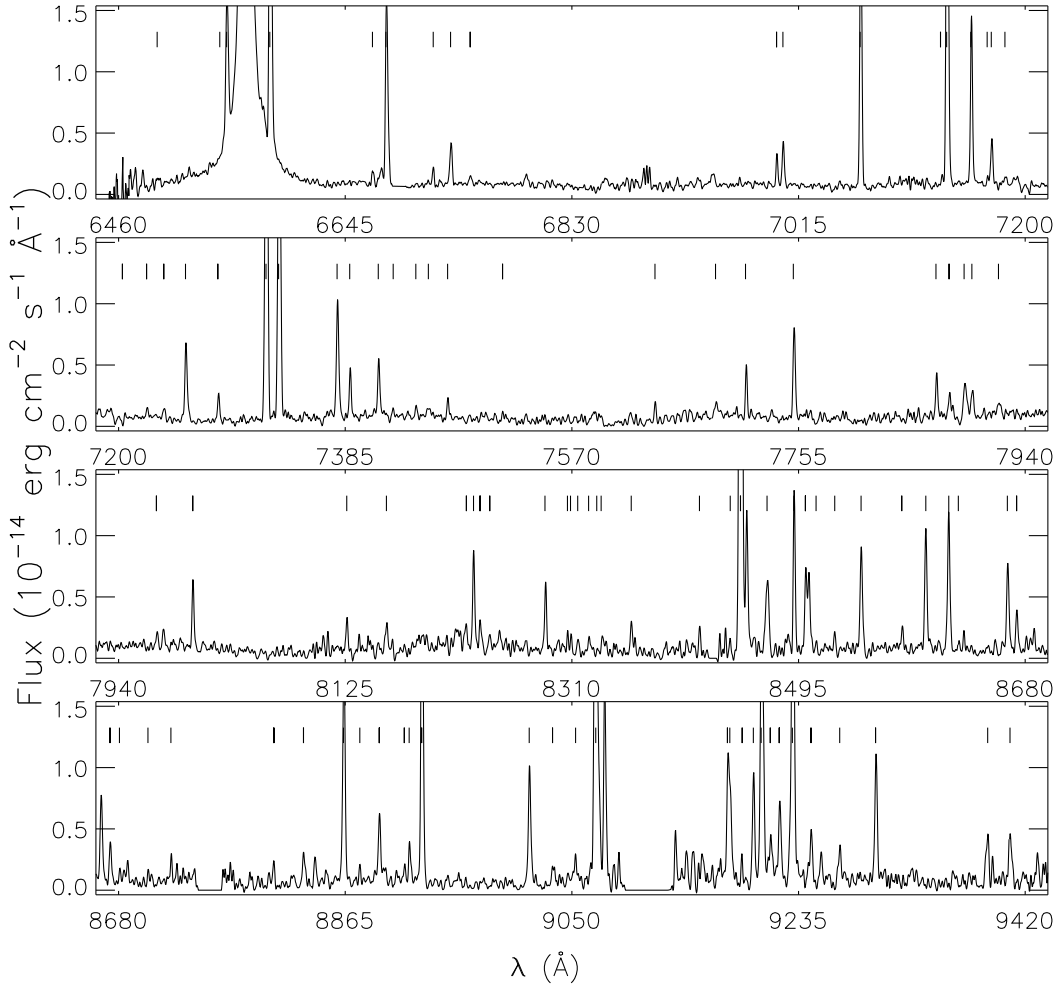
Fig. 5. Red spectrum of the nucleus of M 2-9; it has been expanded to show the faint lines. Also indicated are the identified lines. Our echelle configuration does not cover all the wavelength range, and thus there are gaps in the bottom panel.

sible for the shape of the Balmer profiles, the effect would tend to depend on the wavelength of the lines, and this effect is not observed.

In addition to the observed difference in the shape of the profile of the hydrogen lines, it should be noted that, within the uncertainties, in each series, for increasing energy of the upper level the centroid of the line approaches the systemic velocity. A possible explanation for this behavior in terms of the expected line ratios for each one of the transitions and interstellar extinction will be described in § 3.6.

We compared the hydrogen emission lines in the nucleus with the predictions for Case B recombination (Osterbrock 1989) in an attempt to derive A_V by means of a normal interstellar extinction law.

Assuming a mean density and temperature of 10^6 cm^{-3} and 10^4 K and adopting the interstellar ex-

tinction curve given by Cardelli, Clayton, & Mathis (1989) for $R_V = 3.1$, it is found that while the observed Hα to Hβ ratio suggests $A_V = 6.45$, all other Balmer lines are consistent with $A_V = 1.3 \pm 0.2$. Both estimates are quite different from the value determined by Hora & Latter (1994), $A_V = 2.3$, from the Brackett lines in the nearby IR spectrum of the nucleus. The anomalous value of extinction obtained using the Hα/Hβ ratio can be explained as an exceptionally intense Hα line.

The explanation of the discrepancy between the values of A_V determined by the other Balmer lines and the Brackett lines is less obvious. This discrepancy exceeds all the reasonable uncertainties in line intensity determinations and the possible deviation from Case B recombination. Therefore, this discrepancy suggests an unusual extinction curve.

TABLE 1

EMISSION LINES IN M 2-9 – BLUE SPECTRUM

λ_0	λ_{obs}	$I_\lambda/I_{H\beta}$ [a] observed	$I_\lambda/I_{H\beta}$ [b] ext correct	FWHM Å	Identification
3721.94	3722.04	0.039	0.068	0.9	H 14
3726.03	3726.62	0.058	0.101	0.8	[O II] 1F
3728.81	3729.09	0.040	0.069	1.0	[O II] 1F
3734.37	3734.76	0.013	0.023	0.9	H 13
3750.15	3750.45	0.062	0.107	1.2	H 12
3770.63	3770.87	0.045	0.077	0.8	H 11
3797.90	3798.29	0.044	0.074	0.8	H 10
3835.38	3835.75	0.051	0.086	1.2	H 9
3863.05	3863.22	0.013	0.022	0.8	Ne II
3869.06	3868.96	0.232	0.384	0.9	[Ne III] 1F
3889.05	3889.25	0.183	0.300	1.2	H8
3964.73	3965.29	0.012	0.020	0.4	He I
3967.79	3967.69	0.070	0.112	1.1	[Ne III] 1F
3970.07	3970.49	0.115	0.183	1.1	Hϵ
4026.20	4026.96	0.029	0.045	0.7	He I
4068.60	4069.02	0.038	0.057	0.9	[S II] 1F
4076.35	4076.67	0.019	0.029	1.2	[S II] 1F
4101.73	4102.24	0.230	0.343	1.1	Hδ
4143.76	4144.43	0.009	0.013	1.1	He I
4177.20	4177.82	0.016	0.022	0.7	[Fe II] 21F
4178.85 / 4178.96	{4179.43	0.018	0.026	0.6}	N II / [Fe II]
4233.17	4233.63	0.017	0.024	0.6	Fe II 27
4243.97	4244.68	0.067	0.093	1.4	[Fe II] 21F
4276.83	4277.33	0.045	0.062	0.7	[Fe II] 21F
4287.39	4287.93	0.111	0.151	0.8	[Fe II] 7F
4305.89	4306.36	0.016	0.022	1.0	[Fe II] 21F
4319.62	4320.17	0.032	0.042	0.8	[Fe II] 21F
4326.15 / 4326.24	{4326.94	0.017	0.023	1.0}	[Ni III] 3F / [Ni III]
4340.47	4326.94	0.416	0.531	-	Hγ†
4352.78	4352.21	0.027	0.036	1.2	[Fe II] 21F
4359.33	4359.69	0.099	0.129	1.5	[Fe II] 7F
4363.21	4363.55	0.361	0.468	0.8	[O III] 3F
4372.43	4372.92	0.011	0.014	1.2	[Fe II] 21F
4413.78	4414.36	0.055	0.070	0.9	[Fe II] 7F
4416.27	4416.81	0.057	0.072	0.8	[Fe II] 6F
4452.10	4452.61	0.037	0.046	0.8	[Fe II] 7F
4457.95	4458.59	0.007	0.009	0.9	[Fe II] 6F
4471.50	4471.86	0.062	0.075	0.8	He I
4474.90	4475.43	0.017	0.021	0.9	[Fe II]
4485.21 / 4485.57	{4486.11	0.006	0.008	1.0}	[Ni III] 3F / Fe III
4488.75	4489.39	0.018	0.021	1.5	[Fe II] 6F
4492.63 / 4492.41	{4492.08	0.008	0.010	0.6}	[Fe II] 6F / Ne I
4509.61	4509.47	0.008	0.010	1.6	[Fe II] 6F
4515.34	4515.70	0.020	0.024	1.0	Fe II
4583.84	4584.42	0.029	0.033	0.5	Fe II 38
4607.03	4607.57	0.022	0.025	1.5	[Fe III] 3F
4629.39	4629.95	0.016	0.018	0.9	[Fe II] 37
4639.67	4640.29	0.016	0.018	0.9	[Fe II] 4
4658.05	4658.56	0.136	0.150	1.0	[Fe III] 3F
4701.53	4702.02	0.117	0.126	0.5	[Fe III] 3F
4713.14	4713.61	0.017	0.018	1.0	He I
4728.07	4728.61	0.037	0.040	0.9	[Fe II] 4F
4733.91	4734.28	0.024	0.026	1.3	[Fe III] 3F
4754.69	4755.27	0.024	0.025	1.0	[Fe III] 3F
4769.43	4769.91	0.020	0.021	1.2	[Fe III] 3F
4774.72	4775.34	0.012	0.012	1.1	[Fe II] 20F
4777.68	4778.19	0.012	0.012	1.0	[Fe III] 3F
4814.53	4815.11	0.080	0.082	0.9	[Fe II] 20F
4861.33	-	1.000	1.000	-	Hβ†
4867.95 / 4868.00	{4868.12	0.008	0.008	1.0}	[Fe IV]-F / Ne II
4874.49	4875.12	0.022	0.021	1.0	[Fe II] 20F
4881.00	4881.76	0.018	0.018	2.2	[Fe III] 2F
4900.50	4899.21	0.007	0.007	0.8	[Fe IV]-F
4905.81	4905.86	0.070	0.068	0.2	[Fe II] 20F
4906.36 / 4905.34 / 4906.56	{4906.94	0.029	0.029	0.7}	O II 28 / [Fe III] / [Fe IV]

λ_0	λ_{obs}	$I_\lambda/I_{H\beta}$ [a] observed	$I_\lambda/I_{H\beta}$ [b] ext correct	FWHM Å	Identification
4921.96	4922.42	0.028	0.028	0.9	He I
4923.93	4924.48	0.041	0.040	0.8	Fe II 42
4930.54	4931.13	0.026	0.025	1.1	[Fe III] 1F
4947.37	4947.95	0.011	0.010	2.6	[Fe II] 20F
4950.74	4951.41	0.019	0.018	1.1	[Fe II] 20F
4958.91	-	0.833	0.795	-	[O III]1F†
4973.39	4973.05	0.007	0.006	0.3	[Fe II] 20F
5006.84	-	2.879	2.684	-	[O III] 1F†
5011.25	5011.76	0.072	0.067	1.2	[Fe III] 1F
5015.68	5016.13	0.057	0.053	1.1	He I
5019.29	5019.12	0.017	0.016	0.7	O I 15
5020.23	5020.80	0.025	0.023	0.8	[Fe II] 20F
5032.70	5033.08	0.025	0.023	-	[Fe III] 2F
5033.59	5033.93	0.010	0.009	-	[Fe IV]-F
5041.56 / 5041.40	{5041.94	0.037	0.034	1.5}	[N IV]-F / N I
5043.52	5044.14	0.009	0.009	0.8	[Fe II] 20F
5047.74	5048.43	0.015	0.014	1.3	He I
5055.80	5056.51	0.023	0.021	1.4	Fe I
5060.34	5060.73	0.006	0.005	0.8	[Fe III]
5084.77	5085.36	0.009	0.009	-	[Fe III] 1F
5107.95	5108.59	0.010	0.009	0.9	[Fe II] 18F
5111.63	5112.31	0.031	0.027	1.0	[Fe II] 19F
5147.16	5147.32	0.016	0.014	1.0	[Fe I] 19F
5158.77	5159.28	0.145	0.126	1.2	[Fe II] 19F
5163.95	5164.57	0.022	0.019	1.0	[Fe II]
5169.03	5169.70	0.045	0.039	0.7	Fe II 42
5181.95	5182.63	0.016	0.014	0.8	[Fe II] 18F
5191.82 / 5192.01	{5192.15	0.015	0.013	1.1}	[Ar III] 3F / Ni III
5197.90	5198.34	0.018	0.015	0.6	[N I] 1F
5199.18	5199.77	0.011	0.010	1.0	[Fe II] 35F?
5200.26	5200.84	0.009	0.008	0.6	[N I] 1F
5220.06	5220.80	0.024	0.020	0.8	[Fe II] 19F
5233.76	5234.24	0.014	0.012	0.8	[Fe IV]-F
5234.62	5235.37	0.015	0.013	0.8	Fe II 49?
5261.62	5262.30	0.136	0.113	1.1	[Fe II] 19F
5268.87	5269.50	0.028	0.023	0.5	[Fe II] 18F
5270.40	5270.95	0.189	0.156	1.2	[Fe III] 1F
5273.35	5274.00	0.106	0.088	1.0	[Fe II] 18F
5275.99	5276.66	0.041	0.034	0.8	Fe II 49
5296.83	5297.56	0.021	0.017	1.2	[Fe II] 19F
5333.65	5334.38	0.069	0.055	1.0	[Fe II] 19F
5347.65	5348.33	0.007	0.005	0.8	[Fe II] 18F
5363.30	5363.78	0.014	0.011	1.1	[Ni IV]-F
5376.45	5377.21	0.092	0.073	0.9	[Fe II] 19F
5412.64	5413.08	0.044	0.034	1.4	[Fe II] 17F
5433.13	5433.83	0.026	0.020	0.9	[Fe II] 18F
5477.24	5478.10	0.013	0.010	1.2	[Fe II] 34F
5495.82	5496.56	0.016	0.012	1.7	[Fe II] 17F
5527.33	5528.04	0.065	0.049	0.9	[Fe II] 17F
5534.89 / 5534.70	{5535.55	0.014	0.011	0.9}	Fe II / Ni II
5551.91 / 5551.96	{5552.38	0.008	0.006	1.7}	[Mn II] / [Cr III]
5556.29	5556.54	0.008	0.006	2.3	[Fe II] 18F
5580.82	5581.52	0.004	0.003	1.3	[Fe II] 39F
5613.27	5614.25	0.008	0.006	2.0	[Fe II] 39F
5673.21	5674.13	0.014	0.010	1.1	[Fe II]
5746.96	5747.75	0.035	0.024	1.4	[Fe II] 34F
5754.64	5755.24	0.105	0.072	1.2	[N II] 3F
5773.40	5774.06	0.004	0.002	0.7	[Fe I] 2F?
5780.20 / 5780.51	{5780.72	0.008	0.005	1.7}	Fe II / Ne II
5800.70	5800.81	0.012	0.008	1.6	[Fe IV]-F
5816.02 / 5816.00 / 5816.08	{5816.75	0.007	0.005	1.0}	S II / Mg I / Si I
5835.45	5836.13	0.012	0.008	1.0	[Fe II]
5870.02	5870.81	0.005	0.003	1.4	[Fe II]
5875.67	5876.29	0.595	0.391	1.3	He I 11
5914.61	5914.82	0.004	0.003	-	Ne II

TABLE 1 (CONTINUED)

λ_0	λ_{obs}	$I_\lambda/I_{H\beta}$[a] observed	$I_\lambda/I_{H\beta}$[b] ext correct	FWHM Å	Identification	λ_0	λ_{obs}	$I_\lambda/I_{H\beta}$[a] observed	$I_\lambda/I_{H\beta}$[b] ext correct	FWHM Å	Identification
5957.56	5958.54	0.063	0.040	2.2	Si II 4	6383.72	6384.66	0.009	0.005	0.8	Fe II
5978.93	5979.64	0.059	0.037	1.4	Si II 4	6385.45	6386.25	0.008	0.004	0.6	Fe II
6000.2	6000.60	0.008	0.005	2.0	[Ni III] 2F	6385.64					O I
6046.44	6047.14	0.039	0.024	1.3	O I 22	6440.40	6441.02	0.007	0.004	1.2	[Fe II] 15F
6256.71	6257.68	0.007	0.004	1.3	Si I	6442.95	6443.82	0.005	0.003	0.98	Fe II
6256.93					O I	6456.38	6457.31	0.018	0.010	1.1	[Fe II]
6257.20					C II	6491.28	6492.33	0.023	0.012	-	Fe II
6300.30	6301.10	0.620	0.350	1.0	[O I] 1F	6548.04	6548.82	0.187	0.097	2.0	[N II] 1F
6312.06	6312.68	0.374	0.211	1.2	[S III]	6562.80	-	33.636	17.380	-	Hα[†]
6317.98	6318.88	0.032	0.018	1.1	Fe II	6583.46	6584.20	0.541	0.277	2.0	[N II]
6347.11	6347.87	0.066	0.037	1.6	Si II (2)	6666.80	6667.60	0.034	0.017	0.7	[Ni II] (2D-2F)
6363.78	6364.57	0.166	0.092	0.9	[O I] 1F	6678.15	6678.77	0.303	0.151	1.4	He I (46)
6371.37	6372.09	0.028	0.015	1.2	Si II (2)	6700.64	6702.94	0.010	0.005	0.6	[Fe II]
6371.13					Fe II	6702.22					C II
6379.46	6380.14	0.010	0.005	0.73	Ni II	6716.44	6717.47	0.021	0.010	1.7	[S II] 2F
6380.16					O II	6730.82	6731.75	0.046	0.022	1.7	[S II] 2F

[a]$I(H\beta)_{obs} = 1.50 \times 10^{-13}$ erg cm^{-2} s^{-1}.
[b]$I(H\beta)_{extcorr} = 2.35 \times 10^{-12}$ erg cm^{-2} s^{-1}.
[†]Several components.

The grain distribution of a nebular gas under the presence of a strong radiation field is expected to correspond to grains of larger sizes than those in the typical interstellar medium. This is due to the fact that the small dust grains are easily photodissociated while the large ones are much less affected. A larger grain size results in a shallower extinction curve than that of the galactic interstellar medium. A well known example of this effect is the extinction curve of the Orion Nebula (Mathis & Wallenhorst 1981; Kim, Martin, & Hendry 1994), which is best fitted by $R_V = 5.1$. Besides the R_V variations, the nebula can exhibit an uncommon extinction curve due to the reflection effect and to the mixture of dust grains along the emitting gas column. The dependence on wavelength of the modified extinction curve can be characterized by the nebular extinction parameter, N_V (Bautista, Pogge, & DePoy 1995).

An important characteristic of interstellar extinction is that for λ longer than ~ 1 μm, it is practically insensitive to R_V and N_V. Then, the observations of Hora & Latter (1994) could be real indicators of the amount of extinction in the J band. Starting from their value of $A_V = 2.3$ and $E_{B-V} = 0.75$, a value of $A_J = 0.12$ is obtained. With this fixed value we derive $R_V = 5.0 \pm 0.5$ and $A_V = 2.7 \pm 0.1$ to best represent the optical spectrum. These values were used to correct the observed nuclear lines in our spectrum (Tables 1 and 2).

3.5. Hα line – optical depth effects

Very noticeably in this nebula is that it shows an exceptionally wide Hα profile. Balick (1989) reports a width of 11000 km s^{-1} for this line; Arrieta & Torres-Peimbert (2003) report a full width (FWZI)

of 5000 km s^{-1} that they explain as the result of Raman scattering. The core of the Hα line is also anomalous in that it exhibits at least two strong components with peaks separated by ~ 70 km s^{-1} (see Figure 7).

The Hα/Hβ ratio from the extinction corrected spectrum shows two maxima near –40 and +60 km s^{-1} and a minimum at about –10 km s^{-1}. The ratio at minimum is consistent with the predictions of Case B recombination (value indicated in the bottom panel of Figure 7). On the other hand, the red shifted peak has a ratio about 6 times the value predicted by recombination theory.

Neither collisional excitation nor extinction can explain the large departure from Case B. Instead, the difference can be explained by optical depth effects for transitions to levels n=2. We estimate the optical depth effects by including an escape probability

$$P_{esc} = \frac{1 - \exp(-\tau)}{\tau} \quad (1)$$

on the Balmer lines. Here

$$\tau_{ul} = \text{constant} \times \lambda f_{lu}\left(n_l - \frac{n_u g_l}{g_u}\right)$$
$$\approx \text{constant} \times \lambda f_{lu} n_l, \quad (2)$$

where, f_{lu} is the oscillator strength, n_l and n_u are the populations of the levels involved and g_l and g_u the statistical weights. Then, we compute the H I recombination spectrum using the model of Bautista et al. (1998) assuming that optical depths for all the permitted transitions to level n=1 have an infinitely large value (Case B approximation) and normalizing the optical depth of the Balmer series to that of the
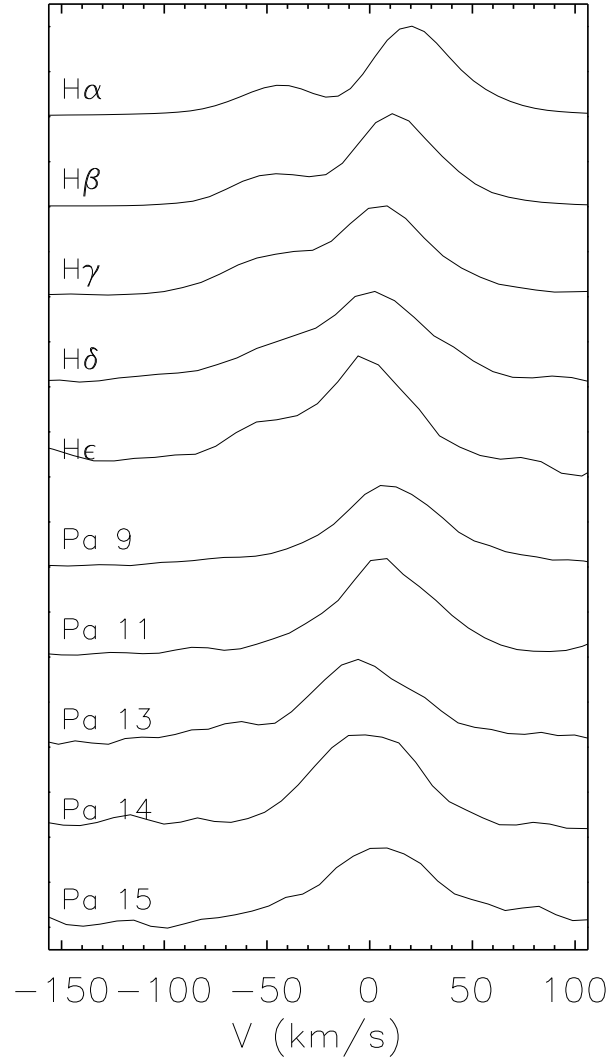
TABLE 2

EMISSION LINES IN M 2-9 – RED SPECTRUM

λ_0	λ_{obs}	$100\times I_\lambda/I_{H\alpha}$[a] observed	$100\times I_\lambda/I_{H\alpha}$[b] ext corrected	FWHM Å	Identification
6548.05	6548.99	0.571	0.573	1.8	[N II] 1F
6562.82	-	100.000	100.000	-	Hα*
6583.46	6584.24	1.747	1.735	1.9	[N II] 1F
6666.80	6668.05	0.104	0.100	1.5	[Ni II] (2D-2F)
6678.15	6678.99	0.765	0.736	1.4	He I (46)
6716.44	6717.65	0.068	0.064	1.6	[S II] 2F
6730.81	6731.81	0.204	0.193	2.1	[S II] 2F
6746.73	{6747.81	0.020	0.018	1.0	[Fe II] (4P-2S)
6746.13					[Fe II]
6997.10	{6997.88	0.094	0.082	1.2	[Fe IV] 4P
6997.18					Fe I
7002.12	7003.07	0.149	0.129	1.6	O I (21)
7065.18	7066.10	0.933	0.792	1.4	He I (10)
7131.11	7131.71	0.041	0.034	1.2	[Fe II]
7135.80	7136.70	1.816	1.506	1.8	[Ar III] (1F)
7155.16	7156.37	0.578	0.477	1.3	[Fe II] (14F)
7169.24	7169.78	0.051	0.042	2.1	Fe II
7172.00	7173.13	0.233	0.191	1.6	[Fe II] (14F)
7182.09	7184.26	0.053	0.043	2.5	O II
7203.90	{7203.96	0.033	0.027	1.8	N II
7203.35					Fe I
7222.18	{7223.69	0.029	0.024	2.1	[Fe II]
7222.80					[Fe IV] (4D-4F)
7236.19	{7237.71	0.061	0.049	1.8	C I
7236.52					Fe I
7254.44	7255.43	0.288	0.230	1.9	O I(20)
7281.35	{7281.83	0.178	0.141	1.6	He I (45)
7281.63					[Fe II]
7131.12	7131.71	0.041	0.034	1.2	[Fe II] (2G-2G)
7319.99	7321.14	2.471	1.931	2.0	[O II] (2F)
7330.73	7331.44	2.510	1.955	2.3	[O II] (2F)
7377.83	7379.16	0.494	0.379	1.8	[Ni II] (2F)
7388.17	7389.47	0.175	0.133	1.5	[Fe II] (14F)
7411.61	7412.79	0.208	0.158	1.6	[Ni II] (2F)
7423.64	7424.97	0.043	0.033	1.6	N I (3)
7442.30	7443.42	0.047	0.035	1.2	N I (3)
7452.54	7453.68	0.188	0.141	1.2	[Fe II] (14F)
7468.31	7469.36	0.061	0.045	1.2	N I (3)
7513.16	7514.25	0.043	0.032	1.72	Fe II
7513.21	7514.25	0.175	0.133	1.5	Ca I
7637.54	7638.63	0.067	0.047	1.5	[Fe II] (1F)
7686.94	7688.06	0.067	0.046	1.7	[Fe II] (1F)
7711.43	7712.52	0.202	0.139	1.1	Fe II
7751.12	7751.58	0.484	0.330	2.4	[Ar III] (1F)
7866.55	7867.97	0.204	0.134	1.60	Fe II
7874.25	{7878.68	0.161	0.105	2.8	[Fe II]
7878.05					Mg II
7889.10	7890.95	0.255	0.166	2.7	[Ni III] (1F)
7896.29	7897.31	0.167	0.109	2.9	[Fe II]
7917.80	7919.00	0.110	0.071	1.9	Fe II
7971.6	{7971.51	0.071	0.045	1.4	He I
7970.61					C III
8000.08	{8001.15	0.192	0.121	1.5	[Cr II] (1F)
7999.49					[Fe II]
8125.30	8126.87	0.061	0.037	1.4	[Cr II] (1F)
8158.13	8159.24	0.098	0.059	1.70	Fe I
8223.13	{8224.49	0.104	0.061	1.6	N I (2)
8222.04					[Fe II]
8229.67	8230.35	0.249	0.147	1.1	[Cr II] (1F)
8235.35	{8235.68	0.098	0.058	2.1	O I
8235.00					Mg I
8235.69					Mg II
8242.39	{8243.58	0.047	0.028	1.3	N I (2)
8242.44					Fe I
8286.43	8288.67	0.273	0.158	1.3	H I
8306.11	8306.99	0.098	0.056	1.4	H I Pa27
8308.49	8309.51	0.131	0.076	1.1	[Cr II] (1F)
8314.26	8315.35	0.084	0.048	1.4	H I Pa26
8323.42	8324.26	0.076	0.044	1.5	H I Pa25
8330.59	8330.92	0.029	0.017	1.4	Fe II
8333.78	8334.50	0.029	0.017	1.2	H I Pa24
8357.69	8359.04	0.175	0.099	2.7	[Cr II](1F) + H I Pa22
8413.32	8414.73	0.124	0.069	1.5	H I Pa19
8437.95	8439.88	0.114	0.063	1.85	H I Pa18
8446.48	{8448.25	4.392	2.430	1.6	O I (4)?
8446.12					[Fe II]
8467.26	8469.90	0.510	0.280	2.7	H I Pa17
8490.73	8491.73	0.525	0.287	1.5	[Fe II] (2G-2F)
8499.70	{8501.24	0.376	0.205	1.7	[Ni III]
8500.20					[Cl III]
8500.32					Cl III
8509.66	8509.92	0.035	0.019	1.23	Fe II
8523.66	8525.14	0.047	0.025	1.37	Fe II]
8545.38	8546.67	0.490	0.264	2.0	H I Pa15
8578.69	{8579.84	0.075	0.040	1.6	[Cl II] (1F)
8579.18					Fe I
8598.39	8599.48	0.431	0.229	1.8	H I Pa14
8616.95	8618.22	0.510	0.269	1.5	[Fe II] (13F)
8626.40	8626.05	0.027	0.014	0.7	[Cr II]
8665.02	8666.07	0.343	0.179	1.9	H I Pa13
8672.32	{8673.60	0.184	0.096	1.73	[Fe II]
8672.40					O III
8680.20	8681.34	0.067	0.035	2.0	O II
8703.87	8704.61	0.082	0.042	1.9	[Ni II]
8722.35	8723.35	0.067	0.034	1.02	Fe II
8806.76					Mg I (7)
8805.43	{8807.32	0.131	0.066	1.6	Fe I
8806.06					Fe I
8830.50	{8831.55	0.157	0.078	1.9	He I
8830.70					[Fe III]
8862.79	8864.18	0.827	0.409	1.9	H I Pa11
8876.34	8877.52	0.086	0.043	1.8	Ca I
8885.62					[Fe II]
8884.94	{8893.48	0.194	0.095	1.8	Si I
8890.70					Fe II
8891.91					[Fe II]
8912.63	{8913.84	0.076	0.037	1.2	Fe II
8913.27					Mg II
8916.76	8917.78	0.147	0.072	1.0	Fe I
8926.64	{8927.97	1.229	0.598	1.51	Fe II
8927.40					Ne I
9014.91	9015.80	0.471	0.224	1.7	H I Pa10
9033.50	{9034.82	0.076	0.036	1.5	[Fe II] (13F)
9034.20					C II
9051.95	9053.66	0.118	0.055	1.7	[Fe II] (13F)
9068.9	9070.08	1.961	0.921	2.3	[S III] (1F)
9177.13	{9177.57	0.765	0.350	1.7	Fe I
9178.42					C I
9178.05	9179.52	0.784	0.359	2.4	Fe II
9188.7	{9189.64	0.127	0.058	1.6	Ne II
9188.16					Fe II]
9197.9	9198.72	0.431	0.196	1.9	C II
9205.30	9205.08	0.665	0.302	1.4	C II
9210.24	{9212.54	0.188	0.085	2.8	He I (6/9)
9210.89					Fe II
9219.80					C II
9218.92	{9219.91	0.320	0.145	2.2	Fe II
9218.25					Mg II
9229.02	9230.57	1.584	0.716	2.0	Pa9
9244.26	{9245.77	0.225	0.102	2.3	Mg II (1)
9244.74					Fe II
9267.56	9269.20	0.112	0.050	1.6	[Fe II] (13F)
9297.1	{9298.47	0.431	0.192	1.57	Fe I
9297.1					Fe II
9388.87	9389.99	0.333	0.145	2.8	Mn II
9407.08	9408.22	0.378	0.164	2.1	Fe II

[a] $I(H\alpha)_{obs} = 6.10 \times 10^{-12}$ erg cm^{-2} s^{-1}.
[b] $I(H\alpha)_{extcorr} = 4.40 \times 10^{-11}$ erg cm^{-2} s^{-1}.
* Several components.

3s - 3p transition, which is kept as a free parameter. Figure 8 shows the value of the Hα/Hβ ratio as a function of τ(3s - 2p). It can be seen that the Hα/Hβ ratio increases monotonically by nearly an order of magnitude as τ(3s - 3p) grows from 0 to 10. The figure also shows that the Hγ/Hβ ratio increases with optical depth too, but by a much smaller factor. This explains that traces of the blue shifted compo-

Fig. 6. Balmer and Paschen hydrogen line series in the nucleus of M 2-9. The intensities have been normalized. Hα shows a marked velocity shift, and the Balmer line profiles show two components.

Fig. 7. Evidence that the Hα line is optically thick in the nucleus of M 2-9. In the upper panel the extinction corrected profiles Hα and Hβ ×3 lines are shown. Zero corresponds to the systemic velocity. In the lower panel the Hα/Hβ ratio of the extinction corrected spectra show excesses in Hα at −40 km s^{-1} and +60 km s^{-1}. The uncertainties and the value of the relation for Case B of recombination are shown.

nents and the red shifted components are present in Hβ. These components, however, are much smaller and closer to the center of the line that in the case of Hα.

Furthermore, the excess in Hα line intensity relative to the one predicted for case B can be explained by high optical depths for the transitions of level n=2. Therefore, it is proposed that the different observed components in these lines are the result of a single optically thick line.

Considering the total flux in the Hα, Hβ and Hγ lines it is found that Hα/Hβ = 17.3 and Hγ/Hβ = 0.531 after extinction correction. These ratios can be reproduced by two models of recombination with

approximate τ(3s - 2p) values of 8.0 and 2.0 respectively. A better approximation in all the H I spectrum could require a more detailed treatment of radiation transfer of the lines. In this work we adopt a mean value of τ(3s - 2p) = 5.

The optical depth in the spectrum of H I has an important effect over the emissivities of the predicted lines and therefore also for the derived H^{+} abundance. For example, for τ(3s - 2p) = 5 the emissivity of the Hβ line is reduced by a factor of 2.6 with respect to Case B recombination, then the calculated H^{+} abundance increases by this same factor.

In brief, an extinction law in the nucleus characterized by R_{V} = 5.0 ± 0.5 and A_{V} = 2.7 ± 0.1 is used to correct the nuclear spectrum for extinction. This extinction law corresponds to larger dust grains than those of the typical interstellar medium. The exceptionally high value of the intensity of the Hα line relative to the predicted recombination by Case B is explained by a Balmer line optical depth τ(3s - 2p) ∼ 5. Further, we propose that the double peaked profile of these lines is also due to optical depth effects.
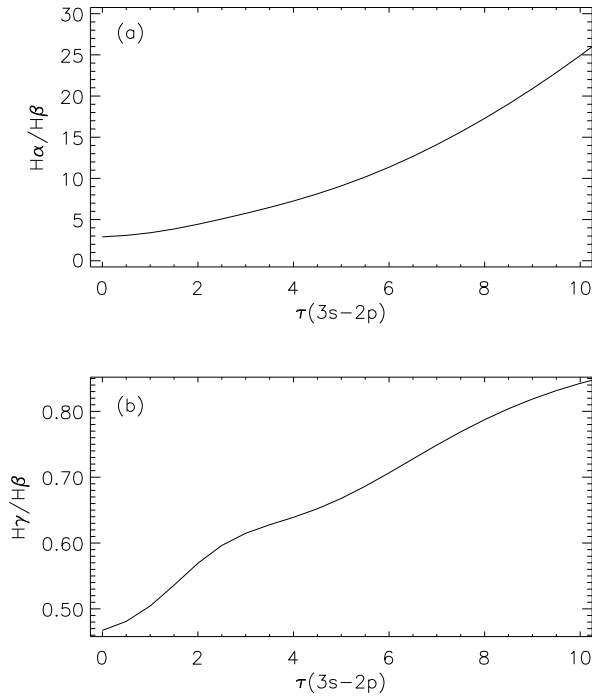
Fig. 8. Dependence on the Balmer intensity ratios on Hα optical depth in the nuclear region of M 2-9. The extinction corrected Hα/Hβ ratio is = 17.3. It is consistent with a value of $\tau(3s$ - $2p) = 8$, while Hγ/Hβ = 0.531 with $\tau(3s$ - $2p) = 2$. In this work a mean value of $\tau(3s$ - $2p) = 5$ was adopted.

3.6. *Forbidden line profiles*

Balick (1989) found that the central region [N II] lines are well characterized by a bright central Gaussian at the systemic velocity, plus two weaker "satellite" lines at about ± 52 km s^{-1}. The bright [N II] emission seen towards the nucleus is "circumstellar". This conclusion is also supported by the very large ratio [N II] 5755/6583 intensities observed towards the nucleus. The circumstellar [N II] lines are spatially unresolved when the slit is oriented E-W (perpendicular to the lobes). Yet, with the slit along the lobes, the two satellite [N II] lines are offset about 0.7″ from the central star. Thus, the satellite lines probably arise along the nebular symmetry axis, and are unlikely to be directly associated to the 2 μm E-W disk surrounding the star observed by Aspin et al. (1988).

Solf (2000) found that [N II] and [O III] in the nuclear region show 3 components of different velocity, the central one at the systemic velocity (low velocity component) and the blue and red shifted components at about ± 50 km s^{-1} (high velocity components), all of which could be resolved spatially along the major axis of the nebula.
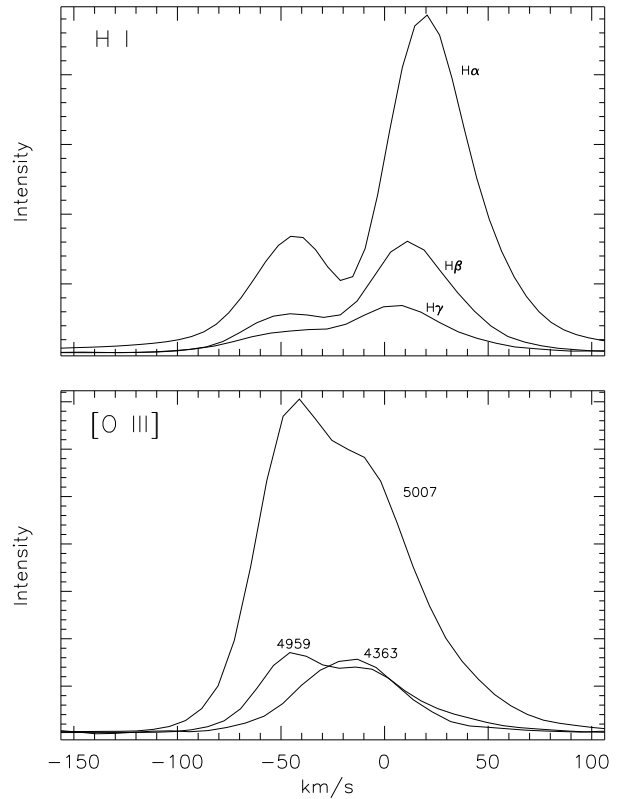
Fig. 9. Comparison of the Balmer series and [O III] profiles in the nuclear region of M 2-9. Both diagrams are on the same velocity scale and are normalized to the maximum of the bright line; on the upper panel Hβ and Hγ have been multiplied by 6. The higher [O III] density corresponds to the central Hα minimum.

We analyze the complex O^{++} emission line profiles in our spectra. While the 5007 and 4959 Å lines present double peaked profiles, with a weak component centered at –17 km s^{-1} and a bright one centered at –45 km s^{-1}, the 4363 Å line shows a single component centered at –17 km s^{-1}. The H I and [O III] profiles are different; whereas for hydrogen the red component is brighter that the blue one, in contrast for oxygen the blue component is stronger than the red one. In Figure 9 we compare the Balmer and [O III] lines on the same velocity scale. The ($\lambda\lambda 5007 + 4959$)/$\lambda 4363$ ratios in the two zones indicate that there is a region with a very high density at –17 km s^{-1} and another of lower density at –45 km s^{-1}. Due to the velocity displacement between the components, it is expected that the higher density component is associated to the region where all the single lines of the spectrum are produced. On the other hand, the blue component is formed in a different region.
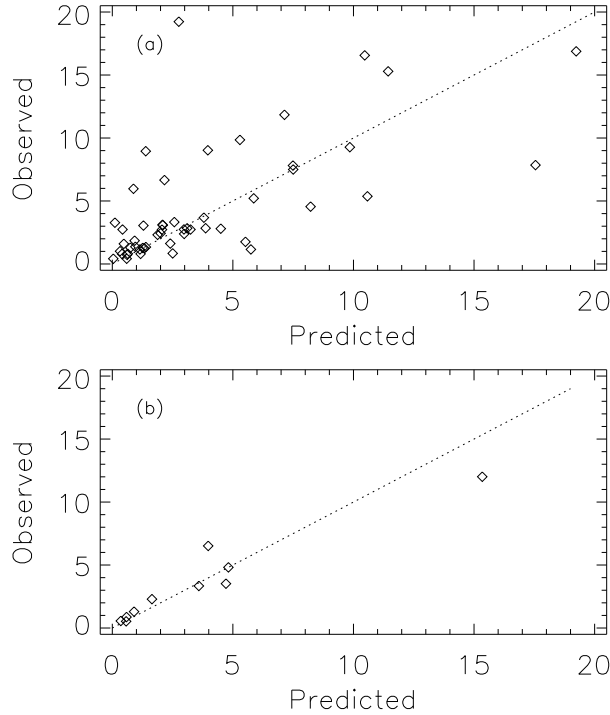
Fig. 10. Observed intensity of the permitted and forbidden Fe II lines vs. the predicted intensities in M 2-9. The predicted lines correspond to a $W = 10^{-9}$, $T_e = 10^4$ K and $N_e = 10^5$ cm^{-3} model. The upper panel corresponds to the lines in the blue spectrum and the lower panel to those of the red spectrum.

3.7. Physical Conditions and kinematics of the emitting region

It has been noted that the low value of [O III] 5007/4363 indicates high densities $\sim 10^{6-7}$ cm^{-3} (Allen & Swings 1972; Goodrich 1991). However, a low density region also contributes to the core; the presence of the [S II] 6717,6731 lines indicates $N_e < 10^4$ cm^{-3}. There is no significant [N I] 5200 emission in the core; the critical density of this line is ~ 2000 cm^{-3}.

In our spectra the [N II], [O II], [O III] and [S II] line ratios were used to determine the temperature and density in the nucleus; for this purpose we applied the NEBULAR tasks of the IRAF data reduction package. In addition, we used models of Bautista & Pradhan (1998) for Fe II, Fe III, and Fe IV, and the model of Bautista (2004) for Ni II.

As it has been mentioned in § 3.6 the [O III] lines also show two components: one centered at –17 km s^{-1} and another at –45 km s^{-1} (see Figure 9). From the $(\lambda\lambda 5007+4959)/\lambda 4363$ line ratio it is found that these components originate in regions of different density. The component at –17 km s^{-1} corre-

sponds to a density $\sim 10^7$ cm^{-3} (that we associate to the nuclear emission proper) while the one at –45 km s^{-1} to $\sim 10^6$ cm^{-3} (that we associate to the micro jets emerging from the nuclear region identified by Balick 1999).

The [Fe II] and [Ni II] lines require special attention. The fact that there are permitted Fe II lines present in the spectrum indicates that this ion is undergoing fluorescence excitation (Bautista & Pradhan 1998). Fluorescence is also suggested by the [Ni II] line intensity ratios, which cannot be reproduced by collisional excitation alone. For the analysis of the [Fe II] lines, those that are less sensitive to fluorescence are selected first; they are usually on the red and infrared part of the spectrum (Bautista & Pradhan 1998). These lines indicate an electronic density of $\sim 10^5$ cm^{-3}. To model the lines affected by fluorescence, the radiation continuum from 0 to 13.6 eV is approximated by a 40,000 K black body spectrum. The intensity of the radiation in the region of the emission line is proportional to the dilution factor

$$W = \frac{1}{4}\left(\frac{R}{r}\right)^2, \qquad (3)$$

where R is the radius of the ionizing star and r is the distance from the emission region to the star. The value of W is adjusted to find the best agreement between predicted relative line intensities and the observed fluxes of Fe II and Ni II lines. It must be noted that variations in the adopted temperature for the black body can be compensated for the most part by different values of W, such that one gets essentially identical fits to the observed spectrum and predicted line emissivities.

In Figure 10 we plot observed Fe II permitted and forbidden intensities against the intensities predicted by the model with $W = 10^{-9}$, $T_e = 10^4$ K and $N_e = 10^5$ cm^{-3}. The upper panel corresponds to the blue spectrum, the lower to the red spectrum. The agreement with the red region is very good while the agreement with the blue region is only moderately satisfactory, although acceptable, given the lower precision of the weak lines and the uncertainties in the radiation field that affects the Fe II lines. However, it should be noted that both forbidden and permitted lines are reasonably well explained with the same model.

Our Fe III model reproduces reasonably well the twelve identified [Fe III] lines in the blue spectrum. The agreement between the model predictions and the observations can be seen in Table 3. Here the mean of the dispersion between the ratio of Fe^{++}/H$^+$ abundance calculated for each line is less that 40%,

TABLE 3

COMPARISON OF OBSERVED AND THEORETICAL [FE III] INTENSITIES NORMALIZED TO $\lambda5085(A\ ^3P_1 - A\ ^5D_0)$

Wavelength	Transition	Obs.	Theoretical
			$I(\lambda)/I(\lambda5085)$
4607	$a\ ^3F_3 - a\ ^5D_4$	2.87	1.84
4658	$a\ ^3F_4 - a\ ^5D_4$	17.2	18.3
4702	$a\ ^3F_3 - a\ ^5D_3$	14.5	9.85
4734	$a\ ^3F_2 - a\ ^5D_2$	2.95	4.05
4755	$a\ ^3F_4 - a\ ^5D_3$	2.91	3.43
4770	$a\ ^3F_3 - a\ ^5D_2$	2.38	3.40
4778	$a\ ^3F_2 - a\ ^5D_1$	1.40	1.96
4881	$a\ ^3H_4 - a\ ^5D_4$	2.11	2.15
4931	$a\ ^3P_0 - a\ ^5D_1$	2.96	2.26
5011	$a\ ^3P_1 - a\ ^5D_2$	7.82	5.83
5085	$a\ ^3P_1 - a\ ^5D_0$	1	1
5270	$a\ ^3P_2 - a\ ^5D_3$	18.5	11.5

which is in accordance to estimated uncertainties in the intensity of these weak lines.

The [Fe IV] lines in the optical spectrum of M 2-9 are consistent with the presence of a high density region. The effective collision strengths for optical [Fe IV] lines are very small; thus, high electron densities are required for those lines to be visible. Table 4 shows the comparison of model predictions with observations. The agreement is excellent for all the lines excepting that at 4906 Å. This disagreement can be due to blends.

We have determined the mean velocity for the different forbidden ions observed. This determination was carried out from those lines that are not ostensibly blended. The observed values are presented in Table 5, where we also include the standard deviation and the number of lines available. In the nuclear

TABLE 4

COMPARISON OF OBSERVED AND THEORETICAL [FE IV] INTENSITIES NORMALIZED TO $\lambda5234\ (A\ ^4F_{3/2} - A\ ^4G_{7/2})$

Wavelength	Transition	Obs.	Theoretical
			$I(\lambda)/\ I(\lambda5233)$
4868	$a\ ^2F_{5/2} - a\ ^4G_{9/2,11/2}$	0.70	0.72
4900	$a\ ^4F_{9/2} - a\ ^4G_{7/2}$	0.57	0.56
4906	$a\ ^4F_{9/2} - a\ ^4G_{11/2}$ $a\ ^4F_{7/2} - a\ ^4G_{5/2}$	2.40	1.72
5033	$a\ ^4F_{3/2} - a\ ^4G_{7/2}$	1	1
5034	$a\ ^4F_{5/2} - a\ ^4G_{11/2}$	0.75	0.74

TABLE 5

RADIAL VELOCITY AND PHYSICAL CONDITIONS OF DIFFERENT IONS FROM FORBIDDEN LINES IN M 2-9

Ion	Radial velocity[a]		$\log N_e$ cm^{-3}	T K	Ionization potential
[N I]	$-11.\pm 4.$	(2)	-	-	0.
[N II]	$-6.\pm 2.$	(3)	5.6	9500	14.53
[N IV]	$-17.\pm-$	(1)	-	-	47.45
[O I]	$-2.\pm 0.$	(2)	-	-	0.
[O II]	$-3.\pm11.$	(4)	5.6	9500	13.62
[O III]	$-17.\pm-$	(1)	7.0	11500	35.12
[Ne III]	$-48.\pm 0.$	(2)	-	-	40.96
[S II]	$-5.\pm 9.$	(4)	5.0	9000	9.98
[Cl II]	$+0.\pm-$	(1)	-	-	12.97
[Cl III]	$-3.\pm-$	(1)	-	-	23.81
[Ar III]	$-15.\pm 9.$	(3)	-	-	27.63
[Cr II]	$-18.\pm21.$	(4)	-	-	7.34
[Fe I]	$-15.\pm11.$	(3)	-	-	0.
[Fe II]	$-1.\pm 8.$	(76)	5.0	9000	7.87
[Fe III]	$-8.\pm 6.$	(14)	6.0	-	16.16
[Fe IV]	$-18.\pm11.$	(6)	6.6	11500	30.65
[Ni II]	$-0.\pm 8.$	(5)	-	-	7.64
[Ni III]	$-10.\pm10.$	(2)	-	-	18.17
[Ni IV]	$-13.\pm-$	(1)	-	-	35.17

[a]Radial velocity and standard deviation. The number of measured lines is shown in parenthesis.

spectrum practically all lines have negative velocities relative to the systemic velocity; they lie in the -48 to $+0.2$ km s^{-1} range. The absence of positive velocity components is an indication of obscuration around the nucleus. The existence of a dense equatorial disk which is obscuring the inner portions of the receding matter has been suggested by Solf (2000). Thus, we can only see the front section of the circumstellar region.

It is also found that there is a relationship between the ionization potential and the radial velocity. This relation is presented in Table 5 and Figure 11 where only those species with more than one observed (unblended) line are displayed. That is, it was found that the velocities for different lines of the same ion are comparable, and that these velocities show a correlation with the ionization potential, where the more negative velocities correspond to higher potentials, and the positive ones to the neutral species. Furthermore, the emission lines originate in regions of a wide range of densities, as presented in this same table. The electron density varies from about 10^5 cm^{-3} in the region of low ionization ([S II] emitting region) to 10^7 cm^{-3} in the [O III] emitting region for temperatures from 9000
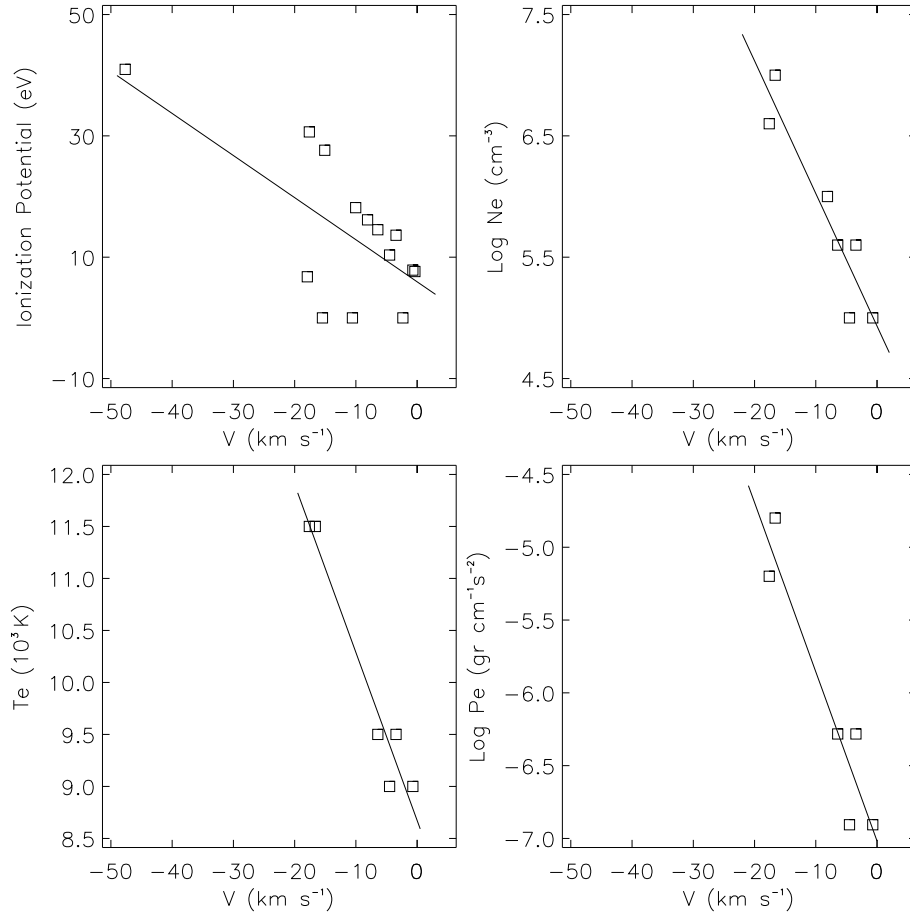
Fig. 11. Behavior of physical conditions relative to the observed radial velocity in M 2-9. On the upper left panel the velocity dependence on ionization potential is shown for those forbidden species for which more than one line was measured. On the lower left panel the electron temperature is presented; on the upper right panel, the electron density; and on the lower right panel, the electron pressure. The velocities are given relative to the systemic velocity. Solid lines indicate the best linear fit to the data.

to 11500 K, respectively. These values are also included in Table 5. This result is in agreement with the Calvet & Cohen (1978) estimates of N_e and T_e determined from the [OIII], [NII] and [OI] lines in the nucleus. They further argue the existence of ionization stratification, where a dense [OIII] zone is surrounded by a less dense [OI] zone. That is, there is also a correlation of physical conditions with radial velocity; where the lines of higher ionization species are emitted in regions of much higher density than those of the neutral species. This dependence is displayed in Figure 11, where we also show evidence of temperature and electron pressure correlation. This well defined negative gradient of ionization potential, electron density, electron temperature and gas pressure with radial velocity was already shown in a preliminary work by Arrieta & Torres-Peimbert (2000).

Although the spectral data reported here refer to a $2'' \times 10''$ window, the observed line emission is produced only in the nuclear region, which is significantly brighter than the surrounding region; that is, we are observing a circumstellar envelope. We adopt a size of the observed circumstellar envelope as that of the [S II] ($\sim 1.5''$ diameter) equatorial region imaged with HST (Figure 1), which at a distance of 650 pc corresponds to a circumstellar structure of ~ 490 AU in radius. The fast moving material (high density, and high ionization), at a mean velocity of ~ 30 km s^{-1}, can traverse the ionized circumstellar region in ~ 80 years.

We try to describe in a very simple manner the geometry of the optical emitting circumstellar region. Comsidering that we observe only negative velocities we rule out the possibility of looking at a complete shell; next we consider the case of the

front half of a spherical shell, in this case the expansion (deprojected) velocities can be 3 times larger than the observed ones; moreover, the profiles would indicate a significant contribution at the systemic velocity. Therefore we find it more likely that we are observing a toroidal geometry, an extension of the molecular torus that is present very close to the star, and extends to large enough distances to pinch the waist of the lobes.

We place the observed high ionization species ([O III], [Ne III], etc.) in the inner part of the torus that is being shocked by the fast wind, and the less ionized species ([S II], [O I], etc.) in the external part, expanding at a lower velocity, consistent with the velocity of the CO torus (~ 7 km s^{-1}). That is, the optical emission lines are produced in the inner regions of the torus that is surrounding the central star. This picture is consistent with a very extended torus where the inner region is producing the optical emission lines and the radio continuum emission (Kwok et al. 1985), followed by the warm H_2 component (observed by Smith et al. 2005), that continues to a CO torus (observed by Zweigle et al. 1997), altogether forming a warm dusty torus at 260 K (Smith & Gehrz 2005).

For the case of a quasi-steady state structure, we can estimate the width of the ionized region of the circumstellar configuration. From conservation of mass considerations the relative sizes of the emitting regions can be derived

$$r_2^2 v_2 n_2 \propto r_1^2 v_1 n_1 \,, \qquad (4)$$

where r_1 and r_2 refer to the internal and external radii of the emitting region. From the values reported in Table 5 and the linear fit presented in Figure 11 we can adopt $v_1 \sim 30$ km s^{-1} and $v_2 \sim 5$ km s^{-1} as the inner and outer expanding velocities and $n_1 \sim 10^{6.7}$ and $n_2 \sim 10^5$ as the densities. We derive $r_2/r_1 \sim 4.5$. Therefore an estimate of the size of the nuclear emitting region can be determined, which corresponds to $r_2 \approx 490$ AU and therefore to $r_1 \approx 110$ AU.

On the other hand, the small scale of the emitting region (~ 490 AU, allows us to propose that observable changes in the kinematical behavior of optical forbidden lines might take place in timescales of the order of ~ 40 years.

3.8. *Abundances*

The estimate of the nebular ion abundances is generally carried out by adopting a mean value for density and temperature and then calculating the line emissivities for all species. This approximation

TABLE 6

ABUNDANCES IN THE M 2-9 NUCLEUS, AND COMPARISON TO SOLAR ABUNDANCES

X	X^0/H^+	X^+/H^+	X^{++}/H^+	X^{3+}/H^+	X/H	X/H solar[a]
He	...	1.1(−1)			1.1(−1)	8.5(−2)
N	1.0(−5)	4.1(−5)	2.9(−5)	...	8.0(−5)	8.3(−5)
O	2.5(−6)	2.2(−4)	1.3(−4)	...	3.5(−4)	6.7(−4)
Ne	...	...	2.8(−7)	...	...	
S	...	5.9(−6)	5.8(−6)	...	1.2(−5)	2.1(−5)
Ar	...	...	7.7(−7)	...		
Fe	...	5.4(−7)	6.1(−6)	2.6(−6)	9.2(−6)	3.2(−5)
Ni	...	1.8(−8)	4.2(−7)	1.4(−7)	5.8(−7)	

[a]From Grevesse & Sauval (1998).

is reasonable in most cases where all diagnostics for each ion agree within their uncertainty. By contrast, in M 2-9 we find a clear density gradient with distance from the central star. Thus, the ionic abundances were calculated here by adopting a varying density through each emission region while the temperature is kept constant at 10^4 K. In this approximation the density diagnostic has been used for each available ion. The calculated abundances for each ion are listed in Table 6.

The abundances of O^0 and N^0 were computed including the contributions of continuum fluorescence from the model of Bautista (1999). To compute the abundances of Ni III and Ni IV we adopted the models of Bautista (2001) and Meléndez & Bautista (2005), respectively.

The comparison with solar abundances yields $N/O_{M\,2-9} > N/O_{\odot}$; this value is common for this type of objects since the alpha mechanism is transforming C into N. Most of the abundances presented in Table 6 are in reasonable agreement with solar abundance values, with the exception of Fe and Ni. The low abundance of these two elements can be explained by depletion into dust (Georgiev at al. 2006).

4. M 1-91

The extreme bipolar planetary nebula M 1-91 (also known as M 4-15, He 2-437 and PN G061.3+ 03.6) is morphologically very similar to M 2-9. In fact is is even more extreme in its aspect ratio (3.6:1). It is among the most collimated PNe known. Although very similar to M 2-9, its surface brightness is lower and thus has been less extensively studied. A striking difference is that the knots in M 1-91 are point-symmetric, not plane-symmetric like those near the center in M 2-9 (Figure 12).

From deep images it is found that it has a size of $45 \times 4.6''$ (Machado et al. 1996). Carsenty & Solf
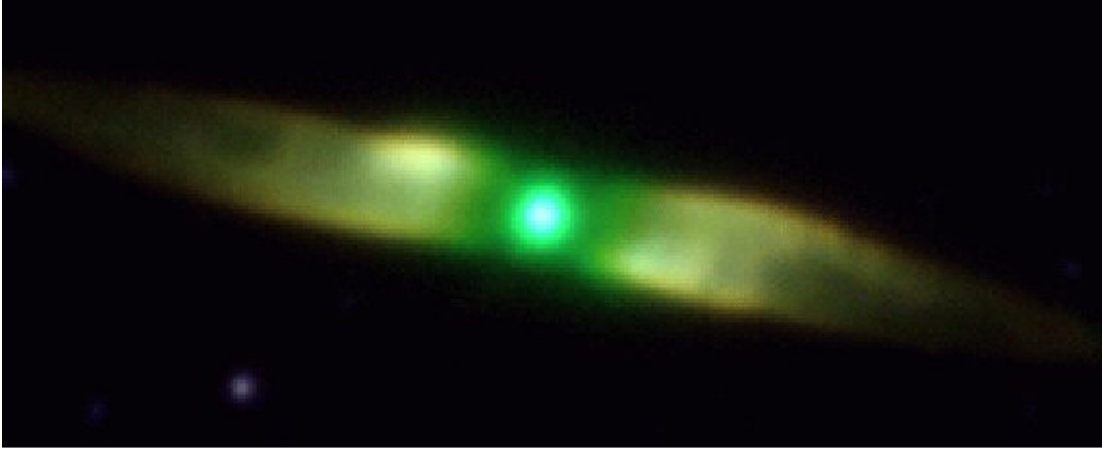
Fig. 12. Image of the planetary nebula M 1-91 (from Manchado et al. 1996). The size is $45 \times 4.6''$. Our slit covered the central $2''$ along the major axis.

(1983) estimate that the inclination angle between the bipolar axis and the plane of the sky is about $15°$. M 1-91 is not only morphologically very similar to M 2-9, but its nuclear spectrum is also quite analogous. It is smaller in size and considerably fainter. Guerrero et al. (2000) detect H_2 only marginally in the lobes of the nebula.

Trammell et al. (1996) report that the lobes are significantly polarized in $H\alpha$. However the high [O III] $\lambda\lambda$ 4959,5007/4363 ratio (~ 89 is the eastern lobe, ~ 67 in the western lobe) compared to the one found in the nucleus (~ 8), indicates that part of the [O III] emission in the lobes is intrinsic and not due to dust scattered from the nucleus (Goodrich 1991).

Calvet & Cohen (1978) estimate a distance of 3.1 kpc for this object, while Cahn & Kaler (1971) and Maciel (1984) estimate a distance to the planetary nebula M 1-91, of 7.79 and 7.0 kpc, respectively; the methods used to determine these values are valid only for optically thin planetary nebulae. As will be discussed later we can conclude that the nucleus of M 1-91 is optically thick, which is another characteristic in common with M 2-9. Rodríguez, Corradi, & Mampaso (2001) adopt a distance for M 1-91 of 7.8 kpc that implies a height above the galactic plane of $z = 440 - 490$ pc, which is still rather high compared to the mean distance to the galactic plane of bipolar planetary nebulae of $<z> = 130$ pc (Corradi & Schwartz 1995); therefore, it is possible that the distance to M 1-91 has been overestimated. There are two ways to determine an approximate distance to this object: (a) by assuming that it has the same physical size as M 2-9, in which case it would be 2.7 times farther away than M 2-9, that is at 1.7 kpc, and (b) by assuming that its height above the galac-

tic plane is 130 pc (the mean value for bipolar PNe), in which case this would correspond to 2.1 kpc. We will adopt a distance of 1.9 kpc for this object.

4.1. Nucleus of M 1-91

The spectrum of the core of M 1-91 closely resembles that of the M 2-9 core (Calvet & Cohen 1978) and $H\alpha$ emission line also shows extended wings (Goodrich 1991). Also like M 2-9, it shows weak [S II] 6717, 6731 and a high [O III] 4363/5007 ratio. The lines of [Fe II] are also seen in M 1-91, although they are relatively weaker than in M 2-9, with somewhat weaker [O III] and iron lines, and stronger [O I] and He I lines.

Rodríguez et al. (2001) estimated densities in the nucleus of M 1-91 to be in the range of $10^{3.3}$ to $10^{6.3}$ cm^{-3} depending on the ion under consideration. They propose that the range in densities indicates that some phenomenon of mass loss or mass motion is taking place in the nucleus.

In contrast to M 2-9 and of most young PNe, the nucleus of M 1-91 does not show a molecular component. Josselin et al. (2000) do not detect CO. The absence of an intense molecular component could be due to a hotter central star in M 1-91.

The radio continuum images only show a compact core, which coincides with the optical stellar core (Lee, Lim, & Kwok 2007). Along the axis they resolve the source to be from 34 to 77 mas, depending on the frequency. The spectral index is of 0.7 which is compatible with an isothermal stellar wind with a constant expansion velocity. Lee et al. (2007) for an isotropic mass loss, derive a mass loss rate of $\dot{M} \sim 9 \times 10^{-5}$ $M_\odot$ yr^{-1}. However, they revise this value by proposing that this source is elongated pos-
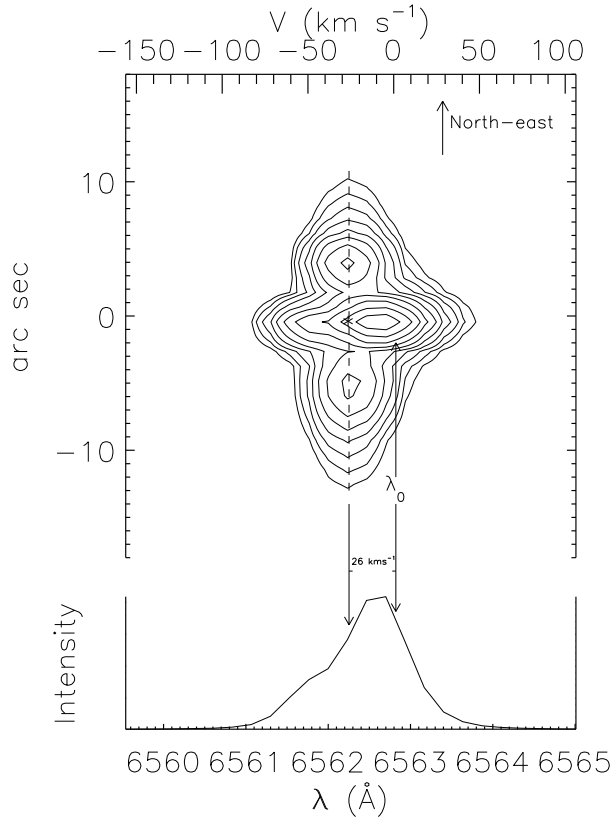
Fig. 13. Determination of the systemic velocity of M 1-91. The dashed line joins both condensations and from it we derive the velocity at the nucleus. The velocity difference is –26 km s^{-1} for the systemic velocity, which corresponds to a heliocentric velocity of -10 ± 5 km s^{-1}.

sibly by collimated winds; in this case it corresponds to $\dot{M} \sim 10^{-6}$ $M_{\odot}$ yr^{-1}. The mass loss rate derived is at least an order of magnitude higher than expected, which they take as an indication that the object is a symbiotic star. They suggest that the radio core represents a collimated outflow responsible for shaping the bipolar morphology of the nebula.

4.2. Systemic velocity

Our slit was located along the major axis, and covered most of the nebula. Also in this case, no significant continuum was measured nor any absorption lines were detected in the spectrum of the nucleus of M 1-91; therefore the systemic velocity determination was carried out under the assumption that the nucleus has the same velocity as the lobes.

Figure 13 shows isocontours on the position-velocity diagram of the long slit echelle spectrum at Hα. Here a very bright central region with a double peaked profile is seen, as well as the eastern and

western lobes. The arrows indicate the laboratory wavelength of Hα, (λ_0) and the position of the central part of the nebula. The difference in velocity of the arrows is $\sim -26 \pm 5$ km s^{-1}. Correcting for the earth's motion ($+16.5$ km s^{-1}) it is found that the heliocentric velocity of the M 1-91 system is -10 ± 5 km s^{-1} and the $V_{\mathrm{LSR}} = +9 \pm 5$ km s^{-1}. In the following sections all the discussions of velocities are referred to the systemic velocity of the nebula.

4.3. Spectrum description

Motivated by the similarity of their spectra the same type of study as performed for M 2-9 and described in § 3.1 was carried out for M 1-91. Unfortunately it is significantly fainter, and thus it was not possible to derive as much information as for M 2-9. The following results are based on our spectral observations of the nuclear zone. Details of the observations and reductions have been given in § 2.

As in the case of M 2-9, the nucleus of M 1-91 shows a faint continuum without absorption lines; however the number of emission lines is more limited. The blue spectrum from 4150 to 6850 is presented in Figure 14. The emission spectrum shows permitted lines (H I, He I, N I, N II, O I, O II, Ne I, Si I, Fe I and Fe II) and forbidden lines ([N II], [O I], [O II], [O III], [Ne III], [Ar III], [S II], [S III], [Fe II], [Fe III] and [Fe IV]). It was also useful to resort to the code EMILI (Sharpee et al. 2003) to identify the faint lines. The code was used for a set of different temperatures (9000 to 11000) and densities (10^4 to $10^{6.5}$ cm^{-3}). The profiles of the Balmer lines and the [O III] 5007, 4959 lines show different unresolved regions. The M 2-9 and M 1-91 spectra are similar, as far as the signal-to-noise ratio allowed such a comparison. Practically all the M 2-9 emission lines stronger than $I_{\lambda}/I_{H\beta} > 0.05$ are present in M 1-91.

In Table 7 the observed spectral lines are listed: Columns (1) and (2) present the laboratory and observed wavelength of the identified lines; Column (3) shows the extinction corrected intensities relative to Hβ (the details about the extinction law are given in § 4.5); Column (4) lists the FWHI (not corrected for instrumental broadening); and in Column (5) the line identification is given.

4.4. Balmer and [O III] profiles

Analogously to the case of M 2-9 the Balmer and [O III] 5007 and 4959 line profiles show several components. In the Balmer series it can be noticed that Hα shows two well separated components and this separation is less defined with increasing upper level.
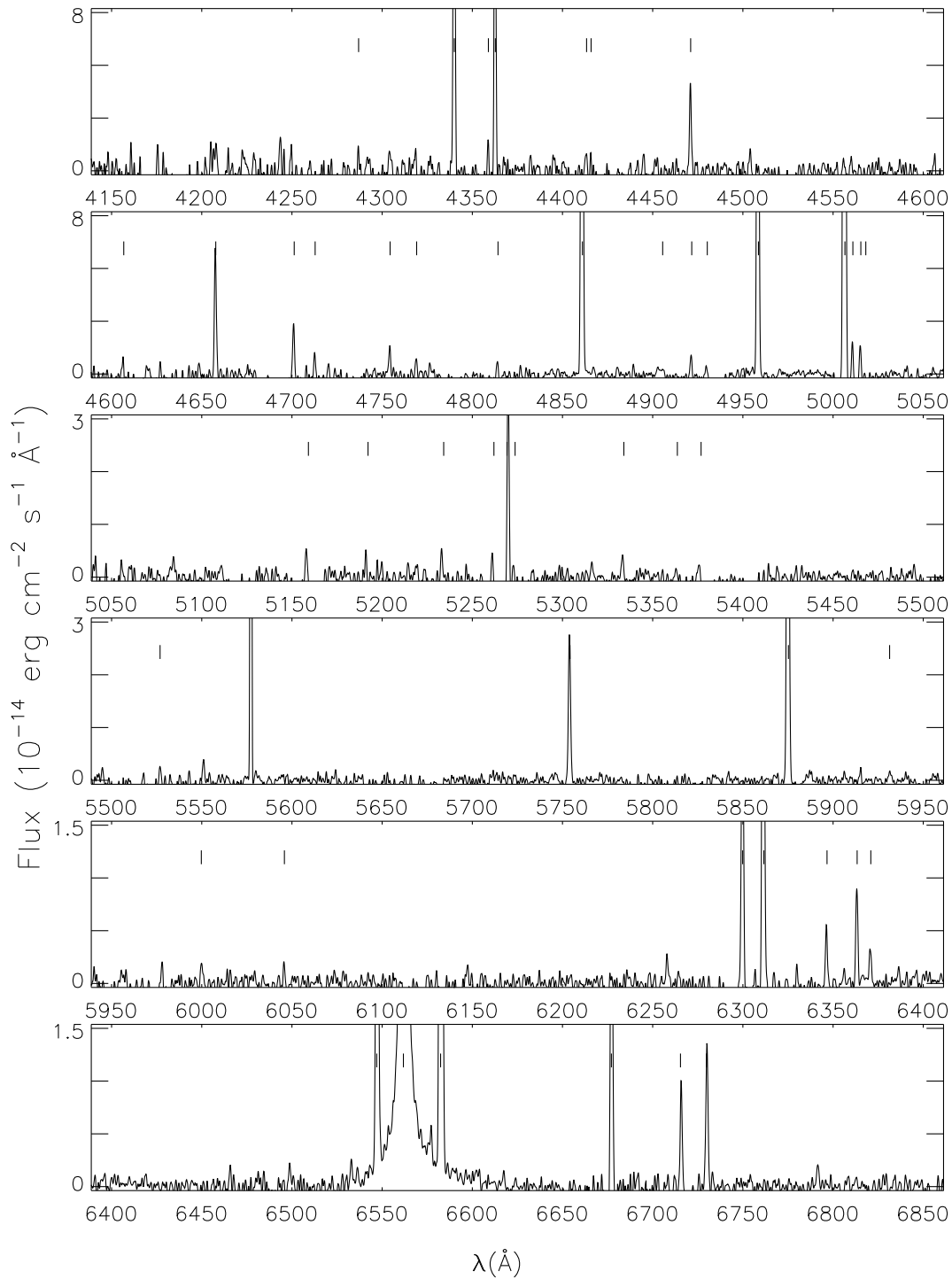
Fig. 14. Blue spectrum of the nucleus of M 1-91. The vertical scale has been expanded to show the faint lines (note that the expansion is different in each panel). The identified lines are marked.

Our M 1-91 spectrum reaches only wavelengths of 6800 Å, and therefore it was not possible to compare the observed Paschen profiles as was the case for M 2-9. In the case of the [O III] lines, the two com-

ponents are not so well separated as in the hydrogen case, but it can be appreciated that the [O III] 5007 and 4959 lines have two components, while [O III] 4363 has a single component. Also, in hydrogen the

TABLE 7

EMISSION LINES IN THE NUCLEUS OF M 1-91

λ_0	λ_{obs}	$I_\lambda/I_{H\beta}$[a] ext corrected	FWHM Å	Identification	λ_0	λ_{obs}	$I_\lambda/I_{H\beta}$[a] ext corrected	FWHM Å	Identification
3721.94	3721.48	0.047	0.5	H14	5158.78	5158.26	0.027	2.0	[Fe II]19F
3726.03	3725.68	0.193	0.6	[O II]	5191.80				O I bl
3728.81	3728.33	0.092	0.5	[O II]	5191.82	{5190.99	0.012	0.9}	[Ar III]3F bl
3734.37	3733.96	0.193	1.2	H13	5233.45				O II bl
3750.15	3749.70	0.130	1.7	H12	5233.76				[Fe IV]F bl
3797.90	3797.37	0.095	1.2	H10	5233.70	{5232.95	0.012	1.0}	N I bl
3869.04	3868.19	0.459	0.8	[Ne III]1F	5234.03				Ne I bl
3889.05	3888.41	0.281	1.3	H8	5261.62	5261.12	0.021	1.1	[Fe II]19F
3967.79	3967.11	0.148	1.3	[Ne III]1F	5270.40	5269.92	0.092	1.1	[Fe III]
3970.07	3969.56	0.193	0.9	Hϵ	5273.35	5272.51	0.003	1.0	[Fe II]18F
4101.73	4101.20	0.311	0.9	Hδ	5333.65	5333.21	0.013	1.6	[Fe II]19F
4287.39	4286.85	0.009	0.7	[Fe II]7F	5363.80	5362.91	0.009	2.1	O II
4340.46	4339.90	0.459	0.9	Hγ	5376.45	5375.90	0.015	1.8	[Fe II]19F
4359.33	4358.79	0.011	0.7	[Fe II]7F	5527.34				[Fe II]17F bl
4363.21	4362.58	0.361	0.8	[O III]3F	5527.57	{5526.81	0.003	1.1}	Fe II bl
4413.78	4413.04	0.047	1.2	[Fe II]7F	5754.64	5753.85	0.061	1.3	[N II]3F
4416.27	4415.79	0.006	0.7	[Fe II]6F	5875.66	5874.95	0.308	1.2	He I
4471.50	4470.90	0.089	1.0	He I	5931.89				Si I bl
4607.03	4606.11	0.025	1.0	[Fe III]3F	5932.35				N II bl
4658.05	4657.53	0.132	1.1	[Fe III]3F	5932.20	{5931.49	0.008	2.1}	Si I bl
4701.53	4700.90	0.061	1.0	[Fe III]3F	6000.55				Fe I bl
4713.22	4712.56	0.027	0.7	He I	6000.93	{5999.94	0.006	1.5}	Ne I bl
4754.69	4754.26	0.030	0.9	[Fe III]3F	6046.39	6045.58	0.005	0.8	O I
4769.43	4768.87	0.022	1.2	[Fe III]3F	6300.30	6299.80	0.068	1.3	[O I]1F
4814.51				O II bl	6312.10	6311.31	0.141	1.2	[S III]
4814.52	{4813.78	0.022	1.2}	[Fe II]20F bl	6347.11	6346.31	0.012	1.1	Si II(2)
4861.32	4860.89	1.000	1.0	Hβ	6363.78	6363.17	0.021	1.2	[O I]1F
4906.00	4905.40	0.003	1.0	O I	6371.37	6370.66	0.008	1.4	Si II(1)
4921.93	4921.22	0.027	1.0	He I	6548.04	6547.30	0.133	1.3	[N II]1F
4930.53	4930.05	0.015	1.8	[Fe III]1F	6562.82	-	7.541		Hα[†]
4958.91	4958.28	0.781	1.0	[O III]1F	6583.46	6582.69	0.441	1.4	[N II]1F
5006.84	5006.20	2.325	1.1	[O III]1F	6678.15	6677.17	0.098	1.3	He I(46)
5011.25	5010.66	0.044	1.1	[Fe III]1F	6716.44	6715.81	0.022	1.2	[S II]2F
5015.68	5015.02	0.033	1.1	He I	6730.81	6730.09	0.031	1.3	[S II]2F
5018.39	5017.49	0.018	1.0	O II					

[a]$I(H\beta)_{obs} = 1.85 \times 10^{-14}$ erg cm^{-2} s^{-1} and $I(H\beta)_{extcorr} = 4.40 \times 10^{-11}$ erg cm^{-2} s^{-1}.
[†]Several components.

red component is stronger than the blue one, in contrast to what is observed in oxygen. These same characteristics are present in the nucleus of M 2-9 (§§ 3.5 and 3.6).

4.5. *Interstellar extinction*

To derive the visual extinction, A_V, the hydrogen emission lines were compared with predictions for Case B recombination using a normal interstellar extinction law.

Assuming a mean density and temperature of 10^6 cm^{-3} and 10^4 K, respectively, and adopting the extinction curve by Cardelli et al. (1989) with $R_V = 3.1$, it is found that while the observed ratio of Hα to Hβ suggests $A_V \sim 5$, all the other Balmer lines are consistent with $A_V = 2.4 \pm 0.3$. The low signal-to-noise ratio in these lines did not allow us to explore the case of an anomalous extinction

curve, as in the case of M 2-9. Therefore, a value of $A_V = 2.4 \pm 0.3$ was adopted from the Hγ/Hβ, Hδ/Hβ, and Hϵ/Hβ ratios. This value was used to correct the spectrum for extinction.

As in M 2-9, the Hα line excess can be explained as an effect of high optical depth to levels n=2. In Figure 15 it is shown that the Hα line exhibits two strong components with peaks separated by ~ 50 km s^{-1}. Observing the Hα/Hβ ratio in this same figure, one finds two maxima of this ratio about -30 and $+40$ km s^{-1} and a minimum centered on the systemic velocity. This ratio in the minimum is consistent with the recombination predictions in Case B (shown in the figure). On the other hand, the highest value of the Hα/Hβ ratio is about 3 times higher than predicted from case B recombination theory.

Comparing the total extinction-corrected Hα and Hβ flux it is found that Hα/Hβ = 7.5. This ratio can
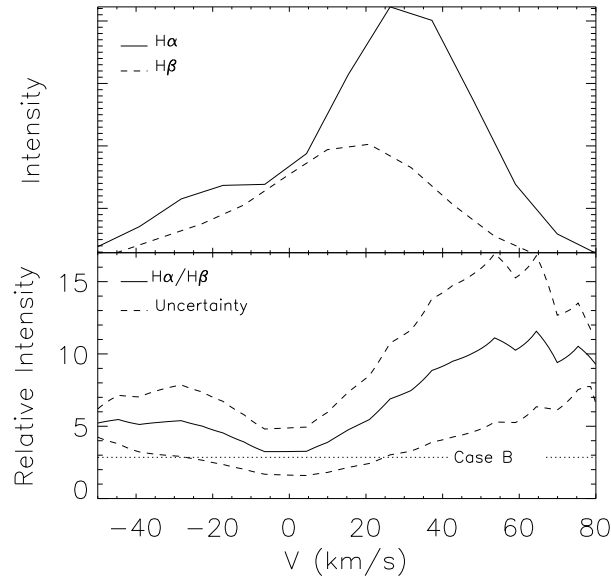
Fig. 15. Hα and Hβ ×3 in M 1-91. The extinction corrected profiles of Hα and Hβ ×3 in M 1-91 are shown in the upper panel. The velocity is given relative to the systemic velocity. In the lower panel the extinction corrected Hα/Hβ ratio is shown. At –30 km s^{-1} and +40 km s^{-1} excesses of the Hα/Hβ ratio can be appreciated. The uncertainties are marked, and the recombination case B value is also included. This diagram is evidence that the Hα line is optically thick.

be reproduced with a case B recombination model with $\tau(3s - 2p) \sim 4$ (as derived from Figure 8).

4.6. *Physical conditions and kinematics of the emitting region*

The forbidden line ratios were used as density diagnostics, applying the NEBULAR tasks of IRAF. The [O II] and [S II] density determinations were obtained from 3729/3726 and 6717/6731 ratios, respectively. The [Fe II], [Fe III], [N II] and [O III] densities were taken from the work by Rodríguez et al. (2001).

The electron density varies from about 2200 cm^{-3} in the region of low ionization ([O II] emitting region) to 3×10^6 cm^{-3} in the [O III] emitting region (Table 8).

All of the forbidden lines show negative velocities, which are indicative of an obscuring disk around the core. The estimate of the velocity for different ions where more than one line is observed is in the -33 to 0 km s^{-1} range relative to the systemic velocity. These velocities show a correlation with the ionization potential, where the more negative velocities correspond to higher potentials, and the positive ones to the neutral species.

TABLE 8

RADIAL VELOCITY AND PHYSICAL CONDITIONS OF DIFFERENT IONS FROM FORBIDDEN LINES IN M 1-91

Ion	Radial velocity[a]		log N_e cm^{-3}	Ionization potential
[N II]	$-11.\pm 3.$	(3)	5.15^b	14.53
[O I]	$-0.\pm 3.$	(2)	–	0.
[O II]	$-7.\pm 5.$	(2)	3.5	13.62
[O III]	$-14.\pm 2.$	(3)	6.4^b	35.12
[Ne III]	$-33.\pm 7.$	(2)	–	40.96
[S II]	$-4.\pm 2.$	(2)	3.34^b	10.36
[S III]	$-12.\pm -$	(1)	–	23.33
[Fe II]	$-10.\pm 8.$	(11)	6.0^b	7.87
[Fe III]	$-10.\pm10.$	(8)	6.5^b	16.16
[Fe IV]	$-20.\pm -$	(1)	–	30.65
[Ar III]	$-22.\pm -$	(1)	–	40.74

[a]Radial velocity and standard deviation. The number of measured lines is shown in parenthesis.
[b]Rodríguez et al. (2001).

There is a correlation between density and velocity in the nuclear spectrum of this object. Again similarly to M 2-9, we find that the behavior of density is not only correlated to the ionization potential but also to the observed radial velocity in each ion. In Figure 16 the relative velocity is plotted for the different species for which we observe more than one line as a function of ionization potential and electron density.

For this object, we also propose that the observed optical emission lines are produced on the front part of the object, while the receding part is obscured by the dense torus. We can only speculate that the ionized region is the inner part of the torus irradiated by the star. We propose that the high density emitting zones are the regions closer to the nucleus, while the neutral or those of lower degree of ionization are at larger distances from the star.

The size of the core emitting region is difficult to estimate. The 1.3 cm radio continuum observations yield a size of 0.077″ (Lee et al. 2007). However, we can conservatively assume that the total diameter of the ionized circumstellar region is 10 times this value, that is, of $\sim 0.8''$. This size is compatible with the $\sim 2''$ size of the direct images available, which are upper limits to the apparent size. At a distance of 1.9 kpc, 0.8″ corresponds to a radius $r_2 \approx 760$ AU. At the mean velocity of 33 km s^{-1} the distance from the star to the outskirts of the ionized circumstellar
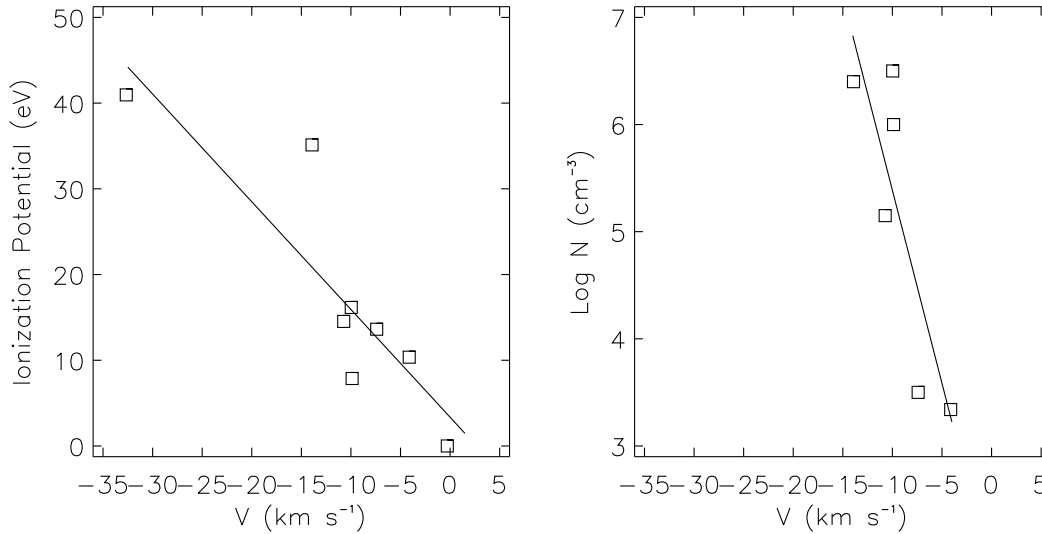
Fig. 16. Behavior of the observed radial velocity with ionization potential and density for M1-91. On the left panel is presented the kinematical behavior of the observed radial velocity with ionization potential in the observed forbidden lines, for which more than one line was measured. On the right panel the electron density behavior with observed radial velocities is displayed. The velocities are given relative to the systemic velocity. The solid line indicates the best fit to the data.

torus can be crossed in 115 years. Then it is conceivable that detectable changes in the kinematical behavior of the system can be expected in a fraction of this time. We suggest that in ~ 30 years there might be significant changes in the velocity distribution of the emitting region.

Alternatively, in the case of quasi-equilibrium, where we assume that constant mass loss is occuring and deceleration of the wind takes place, we can assume that the equation 4 is valid. For the high and low velocities $v_1 \sim 33$ km s^{-1}, and $v_2 \sim 5$ km s^{-1}, and for $n_1 \sim 10^{6.5}$ cm^{-3}, and $n_2 \sim 10^{3.3}$ cm^{-3}, we can derive $r_2/r_1 \sim 32$. For $r_2 \approx 760$ AU (low ionization region) we obtain $r_1 \approx 50$ AU (high ionization region), which would be the inner region where the fast wind is impinging on the dense torus.

5. SUMMARY AND CONCLUSIONS

For M2-9 from the hydrogen Balmer and Paschen series in the nucleus, it was found that the extinction curve has unusual characteristics, different from those of a gas under the action of a strong radiation field. This curve is described by $R_V = 5.0$, $A_V = 2.7$ and explains the discrepancies reported in the literature. The double peak found in the profiles of the Balmer lines had been previously explained by accretion discs like those found in symbiotic stars. According to those models the localized condensations in the disc produces the bright peak in the profile. As the hot spot rotates about of the star, the bright

peak in the profile is blue and red shifted. In this work, the possibility that a fast moving hot spot in an accretion disc produces the asymmetry found in these profiles is not favored; this is based on observations of this object carried out at different epochs, only for the purpose of monitoring the profile morphology. It was found that in all spectra (including the one reported by Balick 1989) the bright peak is always red shifted and the intensity ratio between both peaks remains unchanged. In this section it was found that the double profile can be associated to optical depth effects. From the Hα/Hβ and Hγ/Hβ line ratios an optical depth of $\tau_{H\alpha} \sim 5$ in the line Hα was estimated. In addition, from the $(5007+4959)/4363$ [O III] line ratio it was found that there are two different zones in the nuclear regions not spatially resolved, a component of very high density and velocity –20 km s^{-1} and another less dense with velocity of –45 km s^{-1}. Here it is proposed that the denser component is associated to the circumstellar torus, while the less dense component corresponds to the collimated structure seen in the [O III] 5007 images obtained with HST by Balick et al. (1997). The forbidden emission lines in the core present negative velocities (including [O III] that has a complex profile); that is, we are only observing the approaching side of the core, and presumably there is obscuring material that does not allow us to see the receding part. From the [S II] and [N II] narrow filter HST observations it was found that in these ions the re-

gion has an extended morphology in the equatorial direction. It is here proposed that this extended region is the one that emits with these peculiar characteristics. The upper limit to the size of the ionized region is that of the [S II] emission region in the HST image ($\sim 1.5''$ in diameter) which at a distance of 650 pc corresponds to 490 AU in radius. We can estimate that the more internal emission zones (for example [O III]) are located at about 170 AU from the exciting star. If the assumptions in this work are valid, the extended emitting zone located in the direction of the equator is composed of expanding material. We propose that the emission lines are produced in an inner extension of the molecular torus located very close to the star, and extending to large enough distances to pinch the waist of the lobes. In our scheme the optical emission lines are produced in the inner regions of the torus that is surrounding the central star. The high ionization species are located in the innermost region where the gas is being shocked by the fast wind, and the less ionized species in the external part. The expansion rate of the neutral species is consistent with the low velocity of the CO torus. This scenario corresponds to a very extended torus where the inner region is producing the optical emission lines and the radio continuum emission (Kwok et al. 1985), followed by a warm H_2 component (Smith et al. 2005), that merges into a CO torus (Zweigle et al. 1997), altogether forming a warm dusty torus at 260 K (Smith & Gehrz 2005). In principle, this scenario is in agreement to the wind interaction models (Mellema 1993; Franco, Tenorio-Tagle, & Bodenheimer 1990) at very close distance to the central star, and is compatible with the radio continuum spectral index that agrees with mass loss from the central star. The size of the circumstellar structure is small and the characteristic times are relatively short (for a structure 490 AU radius the crossing time from the central star outwards at a velocity of 30 km s^{-1} is 80 years, and at the same velocity the distance from the inner border to the outer edge of the ionized region can be reached in 53 years). Thus it would be of interest to monitor the kinematic behavior of the emission lines, for any possible changes in timescales of decades. Furthermore, we suggest that the group of pinched waist planetary nebulae should be investigated to find out if this behavior extends to all of them.

For its part, the core of M1-91 exhibits double peaked Balmer lines profiles. It is proposed that these two components can be explained by large optical depth effects in the hydrogen Balmer lines. From the Hα/Hβ ratio, an optical depth of $\tau \sim 4$ was es-

timated for the Hα line. For M 1-91 we again find a correlation of the kinematics of the forbidden lines similar to that of M 2-9. We further find a tendency for the atoms with higher ionization potential to correspond to denser zones, and to have higher absolute velocities relative to the nucleus, while those ions of lower ionization potential are less dense and have lower velocities relative to the nucleus. Although there are no observations of a molecular component in M 1-91, we extend our interpretation of M 2-9 to this object by proposing that the ionized region is the inner part of an extended torus that has produced such a bipolar morphology. It is estimated that the radius of the [S II] circumstellar emitting region is ~ 760 AU (assuming a distance to the nebula of 1.9 kpc). On the one hand, by assuming a quasi equilibrium mass flow in this region it is found that the distance from the nucleus to the inner edge of the circumstellar torus (corresponding to the [Ne III], [O III] emitting region) is ~ 50 AU.

In conclusion, as has been noted by many authors, M 2-9 and M 1-91 indeed share many characteristics: very young emission nebulae of extremely collimated morphology, undisclosed characteristics of the exciting star(s), very dusty circumstellar regions, very high density cores that give rise to Hα Raman scattering, complex Hα profiles, similar nuclear spectra with permitted and emission lines that show the same kinematic behavior, and expanding circumstellar tori that presumably extend to produce the pinched waist. The sizes of the circumstellar structures are small and the characteristic times are relatively short, such that it would be of interest to monitor the kinematic behavior of the emission lines for possible changes that could presumably take place in timescales of decades. Furthermore, we suggest that the cores of the group of pinched waist planetary nebulae should be studied spectroscopically to find out if the emission line kinematics extends to all of them, and if that is the case, to monitor their behavior in time.

Note added in proof: R. Corradi (private communication) kindly informed us that the distance of 650 pc assigned to M 2-9 (Schwarz et al. 1997) is not correct, and that it should be 1.3 kpc. This value, if confirmed, would modify our size and time estimates by a factor of 2.

REFERENCES

Allen, D. A., & Swings, J. P. 1972, ApJ, 174, 583

Arrieta, A., & Torres-Peimbert, S. 2000, in ASP Conf. Ser. 199, Asymmetrical Planetary Nebulae II: From Origins to Microstructures, ed. J. H. Kastner, N. Soker, & S. Rappaport (San Francisco: ASP), 255

_____. 2003, ApJS, 147, 97

Aspin, C., McLean, I. S., & Smith, M. G. 1988, A&A, 196, 227

Balick, B. 1989, AJ, 97, 476

_____. 1999, in ASP Conf. Ser. 188, Optical and Infrared Spectroscopy of Circumstellar Matter, ed. E. Guenther, B. Stecklum, & S. Klose (San Francisco: ASP), 241

Balick, B., Icke V., & Mellema, G., 1997, STScI Press Release PR97-38

Bachiller, R., Martín-Pintado, J., & Bujarrabal, V. 1990, A&A, 227, 188

Bautista, M. A. 1999, A&AS, 137, 529

_____. 2001, A&A, 365, 268

_____. 2004, A&A, 420, 763

Bautista, M. A., Kallman, T. R., Angelini, L., Liedahl, D. A., & Smits, D. P. 1998, ApJ, 509, 848

Bautista, M. A., Pogge, R. W., & DePoy, D. L. 1995, ApJ, 452, 685

Bautista, M. A., & Pradhan, A. K. 1998, RevMexAA (SC), 7, 163

Cahn, J. H., & Kaler, J. B. 1971, ApJS, 22, 319

Calvet, N., & Cohen, M. 1978, MNRAS, 182, 687

Cardelli, J. A., Clayton, G. C., & Mathis, J. S. 1989, ApJ, 345, 245

Carsenty, U., & Solf, J. 1983, IAU Symp. 103, Planetary Nebulae, ed. D. R. Flower (Dordrecht: Reidel), 510

Corradi, R. L. M., & Schwarz, H. E. 1995, A&A, 293, 871

Doyle, S., Balick, B., Corradi, R. L. M., & Schwarz, H. E. 2000, AJ, 119, 1339

Franco, J., Tenorio-Tagle, G., & Bodenheimer, P. 1990, ApJ, 349, 126

Georgiev, L. N., Richer, M. G., Arrieta, A., & Zhekov, S. A. 2006, ApJ, 639, 185

Goodrich, R. W. 1991, ApJ, 366, 163

Grevesse, N., & Sauval, A. J. 1998, Space Sci. Rev., 85, 161

Guerrero, M. A., Villaver, E., Machado, A., García-Lario, P., & Prada, F. 2000, ApJS, 127, 125

Hora, J. L., & Latter, W. B. 1994, ApJ, 437, 281

Josselin, E., Bachiller, R., Manchado, A., & Guerrero, M. A. 2000, A&A, 353, 363

Kim, S., Martin, P. G., & Hendry, P. D. 1994, ApJ, 422, 164

Kohoutek, L., & Surdej, J. 1980, A&A, 85, 161

Kwok, S., Purton, C. R., Matthews, H. E, & Spoelstra, T. A. T. 1985, A&A, 144, 321

Lee, T.-H., Lim, J., & Kwok, S. 2007, ApJ, 665, 341

Livio, M., & Soker, N. 2001, ApJ, 552, 685

Maciel, W. J. 1984, A&AS, 55, 253

Manchado, A., Guerrero, M. A., Stanghellini, L., & Serra-Ricart, M. 1996, The IAC Morphological Catalog of Northern Galactic Planetary Nebulae (La Laguna, España: Instituto de Astrofísica de Canarias)

Mathis, J. S., & Wallenhorst, S. G. 1981, ApJ, 244, 483

Meléndez, M., & Bautista, M. A. 2005, A&A, 436, 1123

Mellema, G. 1993, Ph.D. Thesis, University of Leiden

Osterbrock, D. E. 1989, Astrophysics of Gaseous Nebulae and Active Galactic Nuclei (Mill Valley: Univ. Science Books)

Rodríguez, M., Corradi, R. L. M., & Mampaso, A. 2001, A&A, 377, 1042

Schmidt, G. D., & Cohen, M., 1981, ApJ, 246, 444

Schwarz, H. E., Aspin, C., Corradi, R. L. M., & Reipurth, B. 1997, A&A, 319, 267

Sharpee, B., Williams, R., Baldwin, J. A., & van Hoof, P. A. M. 2003, ApJS, 149, 157

Smith, N., Balick, B., & Gehrz, R. D. 2005, AJ, 130, 853

Smith, N., & Gehrz, R. D. 2005, AJ, 129, 969

Solf, J. 1984, A&A, 139, 296

_____. 2000, A&A, 354, 674

Swings, J. P., & Andrillat, Y. 1979, A&A, 74, 85

Trammell, S. R., Goodrich, R. W., & Dinerstein, H. L. 1995, ApJ, 453, 761

Trammell, S. R., Kartje, J. F., Hill, J. G., & Dinerstein, H. L. 1996, in ASP Conf. Ser. 97, Polarimetry of the Interstellar Medium, ed. W. G. Roberge & C. B. Doug (San Francisco: ASP), 217

Walsh, J. R. 1981, MNRAS, 194, 903

Zweigle, J., Neri, R., Bachiller, R., Bujarrabal, V., & Grewing, M. 1997, A&A, 324, 624

A. Arrieta: Universidad Iberoamericana, Depto. de Física y Matemáticas, Prol. Paseo de la Reforma 880, Lomas de Santa Fe, México D. F. 01219, Mexico (anabel.arrieta@uia.mx).

M. Bautista: Department of Physics, Western Michigan University, Kalamazoo, MI 49008, USA.

S. Torres-Peimbert: Instituto de Astronomía, Universidad Nacional Autónoma de México, Apdo. Postal 70-264, México, D. F. 04510, Mexico (silvia@astroscu.unam.mx).